MODELING AND TRANSIENT DEGRADATION OF PROTON EXCHANGE MEMBRANE FUEL CELLS

by

Sandip Pasricha

A thesis submitted in partial fulfillment
of the requirements for the degree

of

Master of Science

in

Electrical Engineering

MONTANA STATE UNIVERSITY
Bozeman, Montana

April 2006

APPROVAL

of a thesis submitted by

Sandip Pasricha

This thesis has been read by each member of the thesis committee and has been found to be satisfactory regarding content, English usage, format, citations, bibliographic style, and consistency, and is ready for submission to the Division of Graduate Education.

Dr. Steven R. Shaw

Approved for the Department of Electrical Engineering

Dr. James Peterson

Approved for the Division of Graduate Education

Dr. Joseph J. Fedock

STATEMENT OF PERMISSION TO USE

In presenting this thesis in partial fulfullment of the requirements for a master's degree at Montana State University, I agree that the Library shall make it available to borrowers under rules of the Library.

If I have indicated my intention to copyright this thesis by including a copyright notice page, copying is allowable only for scholarly purposes, consistent with "fair use" as prescribed in the U.S. Copyright Law. Requests for permission for extend quotation from or reproduction of this thesis in whole or in parts may be granted only by the copyright holder.

Sandip Pasricha

April 2006

ACKNOWLEDGEMENTS

I would like to express my gratitude to Dr. Steven R. Shaw for his kind advice and supervision throughout this process. I am highly thankful for the time he spent in this project and his understanding.

TABLE OF CONTENTS

TABLE OF CONTENTS – CONTINUED

LIST OF TABLES

LIST OF FIGURES

ABSTRACT

This thesis presents a model based approach to describe proton exchange membrane (PEM) fuel cell degradation with time. This degradation study involves analysis of voltage and current profiles of PEM membranes under transient load conditions. The data is collected from 80 membranes in an Independence1000 1000W PEM system over the life span of the membrane. The thesis also presents PEM fuel cell models developed and validated on a 500W SR-12 commercial PEM stack. Several static models from the literature are reviewed in terms of physical effects, parameterized for identification, and compared using measured data from the commercial PEM stack. The dynamic model is obtained by extending static current voltage profiles to include temperature dependence, and by dynamically modeling the temperature of the membrane. After inspecting all these models a simplified model is used for analyzing PEM fuel cell degradation and changes in physical phenomena in fuel cell observed over a period of time.

INTRODUCTION

Fuel cells are distinguished by electrolyte technology. For example, the electrolyte in a PEM fuel cell is a polymer ion exchange membrane that conducts protons. The electrolyte in molten carbonate fuel cell (MCFC) is usually a combination of alkali carbonates, and the electrolyte in solid oxide fuel cell (SOFC) is a solid metal oxide [11]. This thesis focuses on PEM fuel cells.

Fuel cell membrane degradation is an essential factor determining fuel cell system reliability in practical applications. A PEM membrane degradation and monitoring set-up is introduced in this thesis that runs membranes in a practical, transient-rich electrical environment. The Avista Independence 1000, a commercially available 1000 W PEM fuel cell system, was selected as the membrane test system. Electrical terminal and temperature profiles are collected for each membrane over its entire life-span. Fuel cells are often tested using unrealistic, DC load conditions [18, 19, 20]. The usefulness of this type of data is limited to constant power application, for example, grid support. The degradation set-up introduced in this thesis use a realistic, transient-rich load waveform. Data collected in this manner is expected to capture real-world transient conditions for small fuel cell installations. Examples include portable electronics, cell phones, laptops, and vehicles. On of the few applications where transients will be less of a concern is in constant power, grid support installation.

This thesis attempts to establish a relation between the modeling of electrical terminal measurements of fuel cells and physical or electro-chemical changes that take place during the degradation of PEM membrane. Accurate electrical terminal models of fuel cells are needed for integration of fuel cells with power electronics, critical loads,

and control systems. However, these fuel cell models must also be supported by low-cost, non-invasive measurements under realistic operating conditions. The models presented in this thesis capture the first-order physical phenomena of a PEM fuel cell, can be identified strictly from electrical terminal measurements, and accurately describe the performance of our fuel cell under transient conditions. These models are validated using experimental data collected from a separate 500W SR-12 fuel cell by Avista labs before applying them to the data collected from the degrdation set-up.

This thesis begins with the development and camparison of fuel cell electrical terminal models. The experimental set-up and data collection procedures for fuel cell models validation follow. A PEM fuel cell membrane degradation monitoring setup is introduced and data is collected over the life span of membrane. Trends are observed in the change of parameters of the validated models for the data collected over a period of time. The thesis concludes with a discussion of results.

FUEL CELL ELECTRICAL TERMINAL MODELING

Accurate electrical terminal models of fuel cells are needed for integration of fuel cells with power electronics, critical loads, and control systems. However, these fuel cell models must also be supported by low-cost, non-invasive measurements under realistic operating conditions. The models presented in this thesis capture the first-order physical phenomena of a PEM fuel cell, and can be identified strictly from electrical terminal measurements.

Fuel cell overview

Fig. 1 shows the operation of a typical hydrogen/oxygen PEM fuel cell. The left side of Fig. 1 is exposed to hydrogen from the fuel source, while oxygen is introduced at the right side of the assembly. Often, the oxygen side is simply exposed to circulating air. On the fuel side of the cell, hydrogen dissociates in the presence of a catalyst into electrons and hydrogen ions. The corresponding half-cell reaction is

$$H_2 \rightarrow 2H^+ + 2e^- \tag{1}$$

The electrons flow through a current collector in close contact with the catalyst to the external circuit. The hydrogen ions flow readily through the polymer electrolyte. On the air side of the cell, oxygen, electrons, and hydrogen ions combine in an energetically favorable reaction to form water, i.e.

$$\frac{1}{2}O_2 + 2H^+ + 2e^- \rightarrow H_2O, \tag{2}$$

with an overall reaction of

$$H_2 + \frac{1}{2}O_2 \rightarrow H_2O. \tag{3}$$

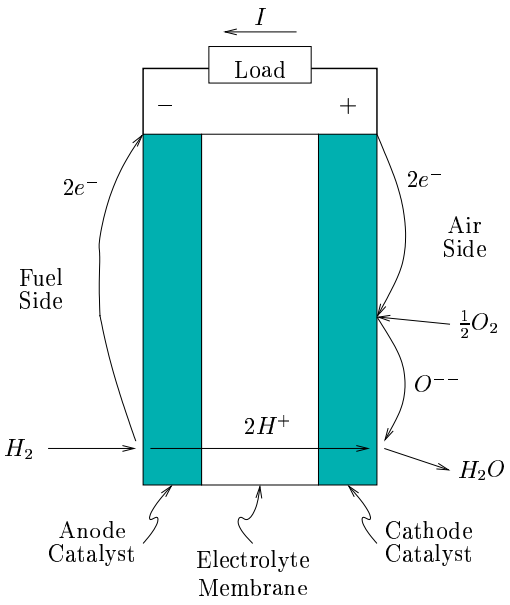

Figure 1: Conceptual diagram of PEM hydrogen/oxygen fuelcell.

The catalyst terminals of the fuel cell are labeled anode or cathode with respect to the ion current flowing in the electrolyte, i.e. the positive ionic current originates at the fuel-side anode and flows through the electrolyte to the oxygen-side cathode. Thus the definitions of the anode and cathode are reversed from the perspective of the electrical load, as positive electrical current flows from the cathode of the fuel cell to the anode. Typically the anode, cathode, and electrolyte in Fig. 1 are laminated or formed together in a thin membrane electrode assembly (MEA).

Fuel Cell polarizations

The open-circuit voltage of a single cell can be computed by consideration of the energies associated with each of the half-cell reactions. For a hydrogen-oxygen cell at 298K, the potential is about 1.2V [9]. The departure from this voltage under load

is associated with loss mechanisms called polarizations. The static models in this thesis capture polarization phenomena in slightly different ways. The purpose of this section is to present the basic effects.

Activation polarization, η_{act} is a loss associated with energy barriers, often associated with the electrodes, that must be overcome for current to flow. Activation polarization at an electrode is often modeled by the Tafel equation,

$$i = i_0 e^{\alpha \frac{F}{RT} \eta_{act}} \tag{4}$$

which is in turn a simplification of the Butler-Volmer equation [9]. In (4), i_0 is the exchange current density, α is the electrode transfer coefficient, and the term $\frac{RT}{F}$ is about 25.7 mV at $T = 298K$. The electrode transfer coefficient is determined experimentally and is often near .5 [9]. An frequently cited interpretation is that $\ln(i_0)$ is the apparent intercept of a Tafel plot of log current density as a function of overpotential, using high-overpotential data for which (4) is valid. The temperature dependence in (4) is slightly misleading. The exchange current density is also temperature dependent, although this is often not explicitly noted. Activation polarization can be compared to the current voltage relationship for a forward-biased diode [10].

Ohmic polarization lumps resistance to both ionic and electronic conduction in the cell, i.e.

$$\eta_{ohm} = IR, \tag{5}$$

where I is the current and R is the cell resistance. Alternatively, ohmic polarization can be expressed in terms of the current density and the area-specific resistance.

Concentration polarization, η_{conc} is due to the consumption of reactants at the anode and cathode. The derivations in [11, 9, 12] assume a linear gradient from the bulk concentration to the electrode surface over a thin Nernst diffusion layer, resulting

in an expression of the form

$$\eta_{conc} = \frac{RT}{nF}\ln(1 - \frac{i}{i_L}). \quad (6)$$

The limiting current density i_L can be thought of as the current corresponding to zero concentration of reactant at the surface [12].

Static fuel cell model

Many steady-state fuel cell models have been developed based on physical and empirical modeling. The comparison of these models will facilitate the understanding of the level of details to be included in a model. The following sub-sections present models from a variety of sources in the original notation. The models are then rewritten in consistent identification forms using the current I and voltage V_{stack} of a stack of N identical cells in series with the goal of modeling the PEM stack in our lab. This convention highlights the parameters we propose to identify when fitting fuel cell current and voltage data. In addition, quadratic and linear models are defined as benchmarks to help assess the relative merit of the more complicated alternatives.

Temperature appears in several of the models. In the experimental setup, a temperature measurement was made as close as possible to the membrane, but in the gradient between membrane and ambient temperature. We attempted to use the temperature model

$$T = (T_{meas} - T_{amb})\mu_7 + T_{amb}, \quad (7)$$

to describe the temperature in each fuel cell model. In (7), T_{meas} represents the measured temperature, T_{amb} is the ambient temperature, and μ_7 is a parameter describing the extent to which the measured temperature lies within the gradient between ambient and internal temperatures.

Fuel Cell Handbook Model

The *Fuel Cell Handbook* [11] provides a physical steady-state model including terms related to the activation, ohmic, and concentration polarizations. The polarizations are explicitly associated with each electrode, and the cell voltage is written as a difference between the electrode potentials. Assuming that the polarizations at the electrodes can be lumped together, the model in [11] is

$$V_{cell} = \Delta E_e - \overbrace{\frac{RT}{\alpha n F}\ln\frac{i}{i_0}}^{\eta_{act}} - \overbrace{iR}^{\eta_{ohm}} + \overbrace{\frac{RT}{nF}\ln(1-\frac{i}{i_L})}^{\eta_{conc}}. \tag{8}$$

This equation is written in terms of the current density, so R in the ohmic term is an area-specific resistance. There is some potential for confusion since R is used as a resistance in the ohmic term and to represent the gas constant in the original notation.

Equation (8) can be written for a stack of N identical cells as

$$\begin{aligned} V_{stack} &= \mu_1 + \mu_2 I + \mu_3 T\ln(I) + \mu_4 T + \\ &\quad \mu_5 T\ln\left(\frac{\mu_6 - I}{\mu_6}\right). \end{aligned} \tag{9}$$

where I is current, T is the membrane temperature and V_{stack} is stack voltage. The μ's are the parameters to be identified. The parameters are related to (8) as follows,

$$\mu_1 = N\Delta E_e \tag{10}$$

$$\mu_2 = -NR\frac{1}{A_{\text{cell}}} \tag{11}$$

$$\mu_3 = -N\frac{R}{\alpha n F} \tag{12}$$

$$\mu_4 = N\frac{R}{\alpha n F}\ln i_0(A_{cell}) \tag{13}$$

$$\mu_5 = N\frac{R}{nF} \tag{14}$$

$$\mu_6 = i_L(A_{\text{cell}}), \tag{15}$$

where A_{cell} represents cell area. Appropriate parameters are scaled by cell area to write the identification form in terms of the total cell current.

This model is similar to the models in [13, 14, 15, 16, 17]. However, the treatment of the concentration polarization differs in [13] and [17]. The model in [13] does not include concentration polarization and the model in [17] uses an empirical logarithmic term to model the concentration region.

Kim et al. Model

An semi-empirical steady-state PEM fuel cell model is developed in [18]. A preliminary model consisting of physically based activation and ohmic polarization terms, as in (4) and (5), is proposed first. The structure of the residual between this model and the observations was found to be exponential, so an exponential term was added. The complete model from [18] in original notation is

$$E = E_o - b\log(i) - iR - me^{ni} \tag{16}$$

where i is current density, m and n are constants. The identification form expressed as a function of current, I for a stack of N identical cells with temperature assumed constant is

$$V_{stack} = \mu_1 + \mu_2 I + \mu_3 \ln(I) + \mu_4 e^{\mu_5 I}. \tag{17}$$

The parameters in identification form are related to the parameters of original equation (16) by

$$\mu_1 = N[E_o + b\log(A_{cell})] \tag{18}$$

$$\mu_2 = -NR \tag{19}$$

$$\mu_3 = -Nb \tag{20}$$

$$\mu_4 = -Nm \tag{21}$$

$$\mu_5 = \frac{n}{A_{cell}}. \tag{22}$$

The parameters μ_1 and μ_5 are adjusted by cell area to express the identification form in terms of current, I instead of current density.

Maggio et al. Model

The model in [19] includes terms for activation, ohmic, concentration polarization and adds a convective polarization term. The convective polarization models losses due to water transport in the membrane. The original source notation in [19] expressed the model as an open circuit voltage minus polarizations, i.e.,

$$V_{cell} = OCV - \eta_{act} - \eta_{ohm} - \eta_{dif} - \eta_{conv} \tag{23}$$

$$OCV = 1.23 - .9 \times 10^{-3}(T - 298) + \frac{RT}{4F}\ln(p_{H_2}^2 p_{O_2}) \tag{24}$$

$$\eta_{act} = \frac{RT}{F}\ln(\frac{I}{I_o}) \tag{25}$$

$$\eta_{ohm} = IR_{cell} \tag{26}$$

$$\eta_{dif} = \omega T I[\ln(\frac{I_{lim}}{I_{lim} - I})] \tag{27}$$

$$\eta_{conv} = Fc_{H^+}v\frac{l_m}{\kappa}. \tag{28}$$

In this model F is Faraday's constant, v is the water velocity in the membrane pores, c_{H^+} is the fixed-charge concentration, l_m is the wet membrane thickness, I_o is the exchange current density, R_{cell} is the cell resistance, ω is the empirical constant for diffusional overpotential, and κ is the membrane ionic conductivity. The diffusional polarization η_{dif} can be compared to the concentration polarization η_{conc} in (8).

The quantities associated with the convective polarization η_{conv} (28) are difficult to measure. However, the water velocity in the membrane pores (v) is related, as in [21], to current such that

$$v = \alpha I + \beta, \tag{29}$$

where α and β are constants in terms of several constant membrane properties with an assumption of constant gas and liquid phase pressure in the cathode and anode gas chambers.

Assuming constant partial pressures of hydrogen and oxygen, (23) through (28) can be rewritten for a stack of N identical cells as

$$\begin{aligned} V_{stack} &= \mu_1 + \mu_2 I + \mu_3 T \ \ln(I) + \mu_4 T + \\ &\quad \mu_5 T I \ln(\frac{\mu_6}{\mu_6 - I}). \end{aligned} \tag{30}$$

The identification parameters are related to equations (23)-(28) by

$$\mu_1 = N[1.49 - F c_{H^+} \beta \frac{l_m}{\kappa}] \tag{31}$$

$$\mu_2 = -N[R_{cell} + F c_{H^+} \alpha \frac{l_m}{\kappa}] \tag{32}$$

$$\mu_3 = -N\frac{R}{F} \tag{33}$$

$$\begin{aligned} \mu_4 &= N[-.9 \times 10^{-3} + \frac{R}{4F} \ln(p_{H_2}^2 p_{O_2}) + \\ &\quad \frac{R}{F} \ln(I_0)] \end{aligned} \tag{34}$$

$$\mu_5 = -N\omega \tag{35}$$

$$\mu_6 = I_{lim}. \tag{36}$$

This model is similar to those in [13, 14, 15, 16, 17] with the exception of the convective polarization term η_{conv}.

Amphlett et al. Model

An empirical model for the Ballard Mark IV PEM fuel cell is proposed in [22], related to a mechanistic model in [23]. The model in [22] is

$$\begin{aligned} V &= E + \eta_{act} + \eta_{ohmic} && (37)\\ E &= 1.23 - .85 \times 10^{-3}(T - 298) + \\ &\quad \frac{RT}{nF}\ln(p_{H_2} p_{O_2}^{1/2}) && (38)\\ \eta_{act} &= \xi_1 + \xi_2 T + \xi_3 T\ \ln(c_{O_2}) + \\ &\quad \xi_4 T\ \ln(i) && (39)\\ \eta_{ohmic} &= -iR^{internal} && (40)\\ R^{internal} &= \gamma_1 - \gamma_2 T + \gamma_3 i && (41) \end{aligned}$$

where the ξ's and γ's are parameters. This model explicitly captures the influence of operating temperature on the polarizations, and includes partial pressure information p_{H_2} and p_{O_2} and oxygen concentration c_{O_2} terms. The symbol i in this original notation is current, not current density.

The identification form including temperature as an independent variable of this model is

$$\begin{aligned} V_{stack} &= \mu_1 + \mu_2 T + \mu_3 T \ln(I) + \mu_4 I + \\ &\quad + \mu_5 IT + \mu_6 I^2. && (42) \end{aligned}$$

The identification parameters are related to equations (37)- (41) by

$$\begin{aligned} \mu_1 &= N[1.48 + N\xi_1] && (43)\\ \mu_2 &= N[-.85 \times 10^{-3} + \xi_2 + \xi_3 \ln(c_{O_2}) + \\ &\quad \frac{R}{nF}\ln(p_{H_2} p_{O_2}^{1/2})] && (44) \end{aligned}$$

$$\mu_3 = N\xi_4 \tag{45}$$

$$\mu_4 = -N\gamma_1 \tag{46}$$

$$\mu_5 = N\gamma_2 \tag{47}$$

$$\mu_6 = -N\gamma_3, \tag{48}$$

The model developed in [22] was used to predict the response of practical fuel cells in [24] and [25]. The general form of the model given in equation (37) is similar to the model in [13].

Chiu et al. Model

The model in [26] includes terms related to activation losses, internal current losses, resistive losses, and mass transport or concentratation losses. Although the original model is a dynamic description, we set the time derivatives to zero to obtain a static model. With this modification, the model from [26] in original notation is

$$E = N\left(E_0 + \frac{RT}{2F}\ln\left(\frac{P_{H_2}(\frac{P_{O_2}}{P_{std}})^{\frac{1}{2}}}{p_{H_2O_c}}\right) - L\right) \tag{49}$$

$$L = (i+i_n)r + a\ln\left(\frac{i+i_n}{i_o}\right) - b\ln\left(1-\frac{i+i_n}{i_l}\right) \tag{50}$$

where E is the stack output voltage, N is the number of cells in stack, E_0 is the cell open circuit voltage at standard pressure, T is the constant operating temperature, and L is the voltage losses. In addition, P_{H_2}, P_{O_2}, and $P_{H_2O_c}$ represent the partial pressure of each gas inside the cell. P_{std} is the standard pressure. Also, i_n is the internal current density related to the internal current losses, i_l is the limiting current density, r is the area specific resistance, and a and b are constants.

The following identification forms assume constant partial pressures P_{H_2}, P_{O_2} and $P_{H_2O_c}$. The identification form expressed as a function of current, I for a stack of N identical cells is

$$\begin{aligned} V_{stack} &= \mu_1 + \mu_2 I + \mu_3 \ln(\mu_4 + I) + \\ & \quad \mu_5 \ln(\mu_6 - I). \end{aligned} \tag{51}$$

The identification parameters are related to equations (49)- (50) by

$$\begin{aligned} \mu_1 &= N[E_0 - i_n r + a \ln(i_o(A_{cell})) - b \ln(i_l(A_{cell}))] + \\ & \quad \frac{NRT}{2F} \ln\left(\frac{P_{H_2}(\frac{P_{O_2}}{P_{std}})^{\frac{1}{2}}}{p_{H_2O_c}}\right) && (52) \\ \mu_2 &= N\left[\frac{-r}{A_{cell}}\right] && (53) \\ \mu_3 &= -Na && (54) \\ \mu_4 &= i_n(A_{cell}) && (55) \\ \mu_5 &= Nb && (56) \\ \mu_6 &= i_n(A_{cell}) + i_l(A_{cell}) && (57) \\ & && (58) \end{aligned}$$

where A_{cell} represents cell area. Also, μ_1, μ_2, μ_4 and μ_6 are adjusted by cell area in order to express the identification form in terms of current, I instead of current density.

Linear and Quadratic Models

The following linear and quadratic identification models are proposed as a benchmark to help assess the relative usefulness of the physical and empirical terms in the

models proposed in [23, 22, 11, 18, 19] for electrical terminal modeling. Assuming the stack voltage is a function of current I and temperature T,

$$V_{stack} = f(I,T), \tag{59}$$

and the Taylor series exists, then it can be written as

$$\begin{aligned} V_{stack} &= f(I_0,T_0) + \frac{\partial f}{\partial I}\tilde{I} + \frac{\partial f}{\partial T}\tilde{T} + \\ &\quad higher\ order\ terms. \end{aligned} \tag{60}$$

where $I = I_0 + \tilde{I}$ and $T = T_0 + \tilde{T}$. Here, $\tilde{I}$ and $\tilde{T}$ are small signal currents and temperatures and I_0 and T_0 are the operating points corresponding to the derivatives. Assuming that higher order terms of the series can be ignored and that $\tilde{I}$ and $\tilde{T}$ are the variables of interest, the identification forms of the linear and quadratic models are

$$V_{stack} = \mu_1 + \mu_2\tilde{I} + \mu_3\tilde{T} \tag{61}$$

and

$$\begin{aligned} V_{stack} &= \mu_1 + \mu_2\tilde{I} + \mu_3\tilde{T} + \mu_4\tilde{I}^2 + \mu_5\tilde{T}^2 + \\ &\quad \mu_6\tilde{I}\tilde{T} \end{aligned} \tag{62}$$

where μ's are the identification parameters. The identification parameters are related to equation (60) by

$$\mu_1 = f(I_0,T_0) \tag{63}$$

$$\mu_2 = \frac{\partial f(I_0,T_0)}{\partial I} \tag{64}$$

$$\mu_3 = \frac{\partial f(I_0,T_0)}{\partial T} \tag{65}$$

$$\mu_4 = \frac{1}{2}\frac{\partial^2 f(I_0,T_0)}{\partial I^2} \tag{66}$$

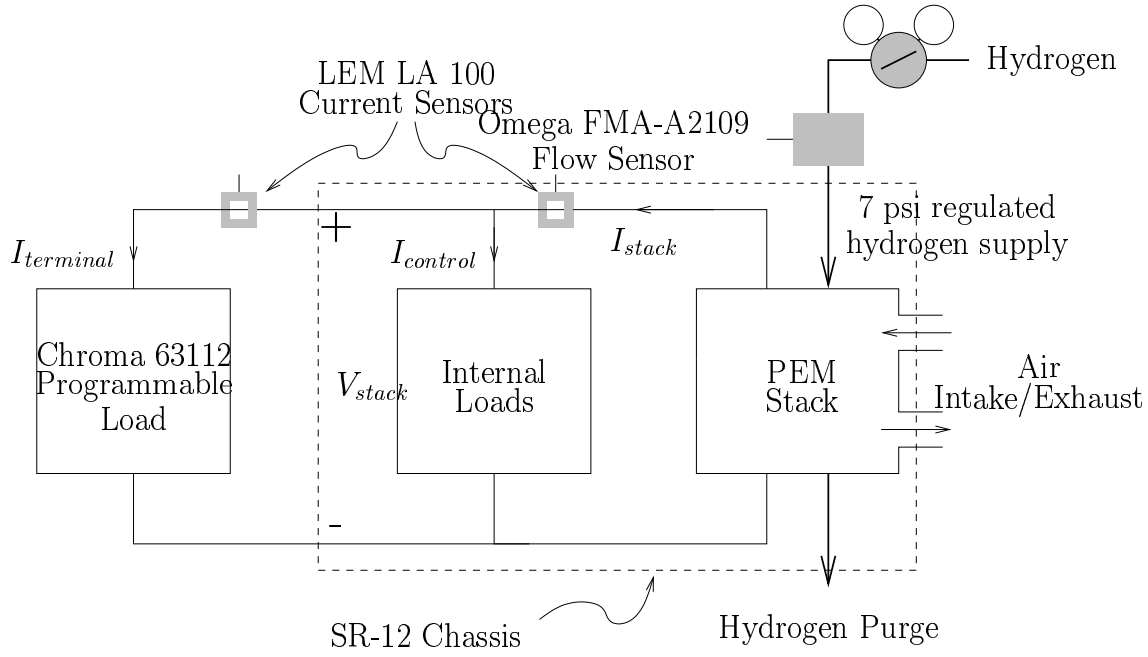

Figure 2: Schematic of experimental setup for dynamic and static tests.

$$\mu_5 = \frac{1}{2}\frac{\partial^2 f(I_0, T_0)}{\partial T^2} \tag{67}$$

$$\mu_6 = \frac{\partial^2 f(I_0, T_0)}{\partial I \partial T}. \tag{68}$$

Experimental setup for validation of static fuel cell models

An Avista Labs SR-12 500W PEM fuel cell was used to obtain data for testing the models. The SR-12 is a self contained unit with a 48 cell PEM stack in 12 removable cartridges in series, plumbing, start-up battery, cooling fan, and control hardware. The SR-12 controls operate off the power generated by the stack, so we model them as an "internal load" in Fig. 2. The cartridges have modular electrical and mechanical connections that allow them to be replaced while running in the event of failure. Each of the twelve cartridges contains four membrane electrode assemblies connected in series. There is a center connection for the four-cell stack in each cartridge, so that

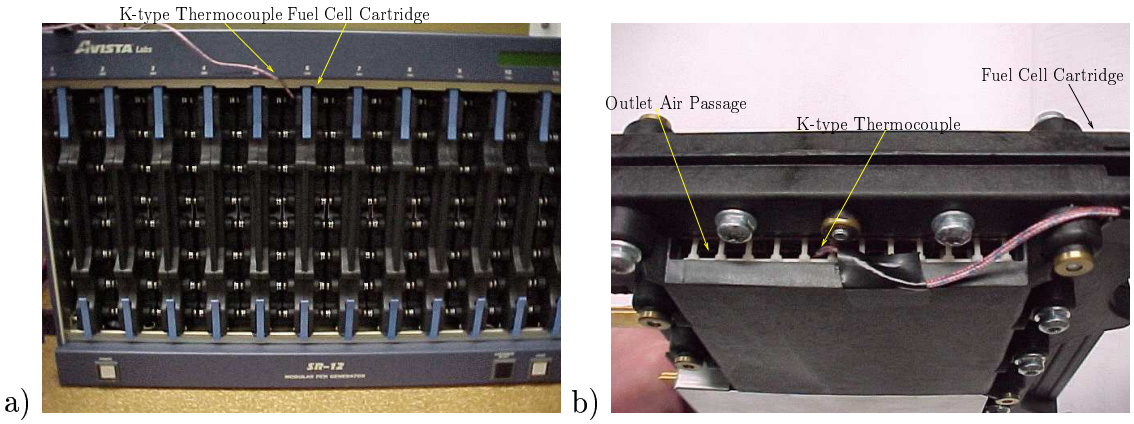

Figure 3: Location of K-type thermocouple in SR-12 fuel cell stack a) and location of thermocouple in the fuel cell cartridge b).

the control unit can access pairs of adjacent membranes. These pairs of membranes are sequentially shorted with MOSFET for about 30ms as part of the operating procedure of the system. As a result, the output voltage fluctuates depending on which membranes are connected to the terminals at any given time.

The SR-12 uses high-purity 99.95% hydrogen delivered at 7 psi. Fuel flow is measured with an Omega FMA-A2109 mass flow sensor. Room air is circulated by fan, controlled by the SR-12, over the oxygen side of the membranes. The fan is under active control. Current was measured at two locations. By disassembling the SR-12 we were able to position an LEM LA-100 active Hall effect current sensor so that it would measure all of the current delivered by the stack. The current delivered to the external Chroma 63112 programmable load was measured by an identical sensor. Stack voltage was measured with an LEM LV25-P isolated voltage sensor. Type-K thermocouples and Omega SMCJ thermocouple signal conditioners were used to measure temperature. One thermocouple was glued to the gas diffusion layer on the air side of the MEA on one of the cartridges. This location is as close to the MEA as possible without disturbing the cartridge. The other thermocouple was placed in

the air outlet of the system. Measurements from all sensors were sampled in 12 bit resolution at 50 Hz with an Advantech PCI-1710 data acquisition card. Fig. 2 shows a schematic of the SR-12 and associated instrumentation.

Steady-state data was obtained by gradually increasing the load current from from 1.1A to 20.5A, incrementing by .2A every 40 seconds. The load for the SR-12 was provided by a Chroma 63112 programmable load operating in constant current mode. The SR-12 was operated under no load conditions for 30 minutes after completing its factory programmed warm-up cycle before collecting data.

Validation results for static model

Fig. 4 shows a sample data set, collected using the quasi-static test procedure with a gradual series of steps in the terminal current. The "step" in stack current near $t = 2500s$ in Fig. 4(a) is due to an increase in the speed of the SR-12's internal fan. There is a corresponding drop in the stack voltage, Fig. 4(b). The operation of the fan also has an effect on the outlet air temperature, Fig. 4(d). The hydrogen flow profile in Fig. 4(c) has a number of "spikes". The SR-12 periodically purges the anode side of the membranes to avoid the accumulation of impurities.

Parameters for each model were estimated using the Levenburg-Marquardt method [27] to minimize the least-square error criterion for stack voltage prediction as a function of stack current and measured temperature. Unfortunately, the quasi-static data as in Fig. 4 do not support independent treatment of temperature and current, as the current profile in Fig. 4(a) and temperature in Fig. 4(d) are very closely related. To avoid this problem, we constrained μ_7 to zero in (7) for all models, and T_{amb} was set to a nominal PEM operating temperature of 353K. In the case of the quadratic and linear models, the coefficients associated with temperature were set to zero.

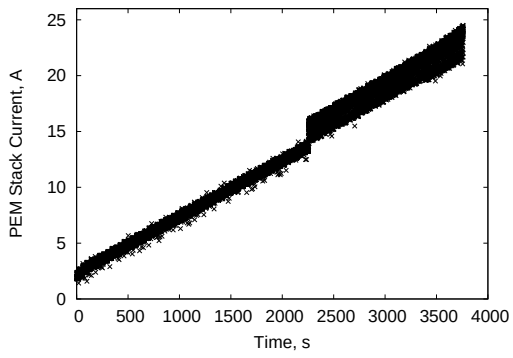

(a) Stack current as a function of time

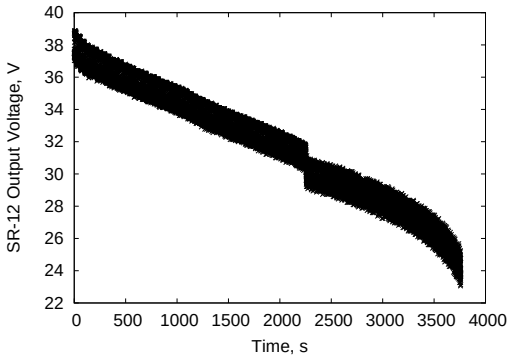

(b) Stack voltage as a function of time

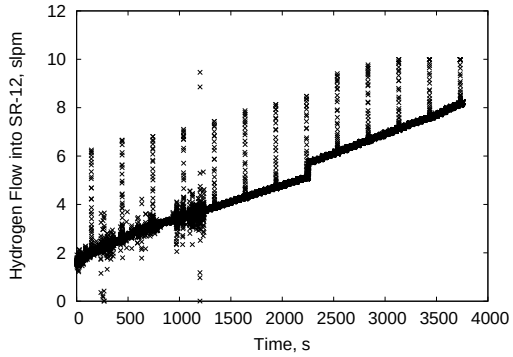

(c) Hydrogen flow at input as a function of time

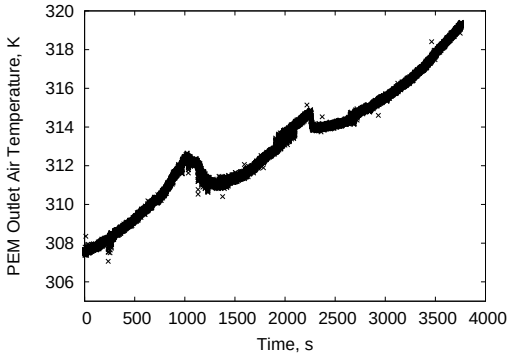

(d) Temperature as a function of time

Figure 4: Stack current, stack voltage, fuel flow and temperature during a typical static test.

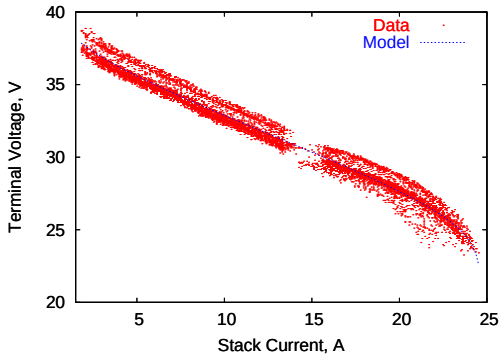

(a) Fuel Cell Handbook

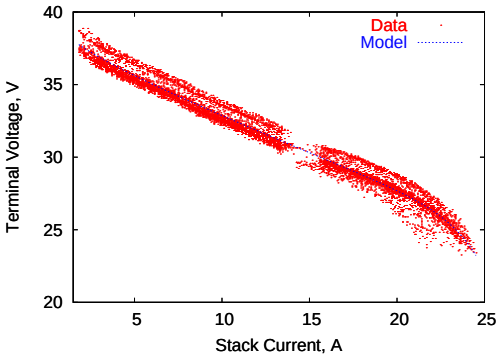

(b) Kim et al.

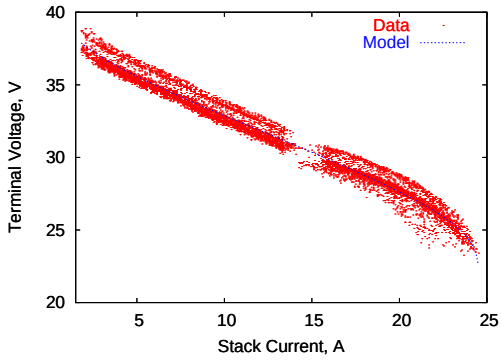

(c) Maggio et al.

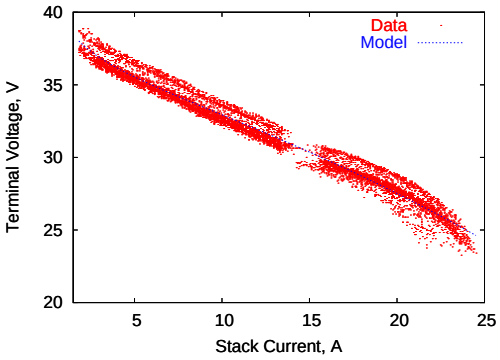

(d) Amphlett et al.

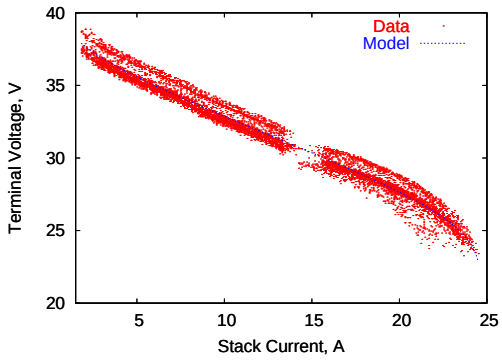

(e) Chiu et al.

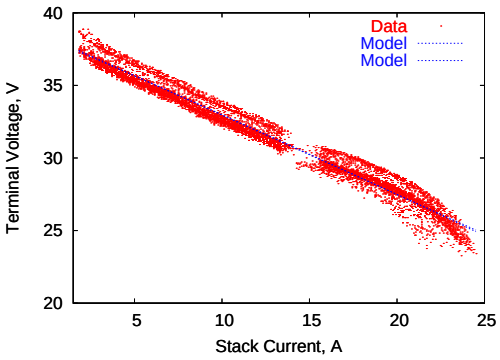

(f) Linear and Quadratic

Figure 5: Measured (dots) and predicted voltage as a function of terminal current using the models in equations (9) in a), (17) in b), (30) in c) , (42) in d), and (51) in e) and using the models in equations (61) and (62) in f).

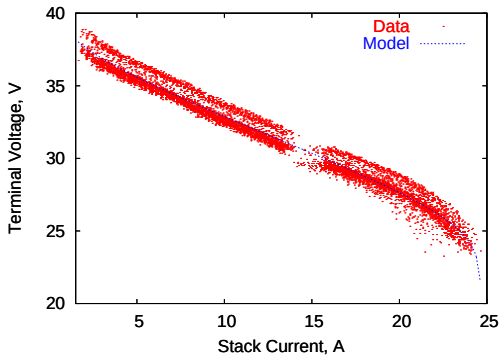

(a) Fuel Cell Handbook

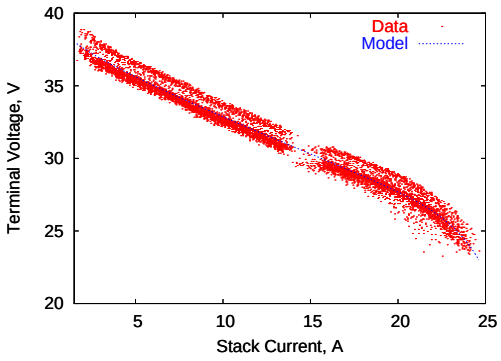

(b) Kim et al.

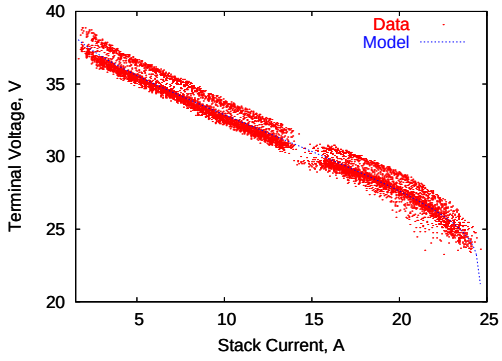

(c) Maggio et al.

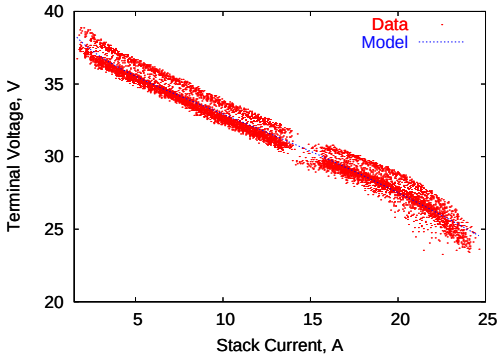

(d) Amphlett et al.

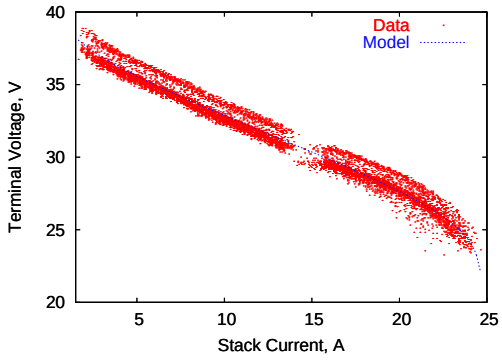

(e) Chiu et al.

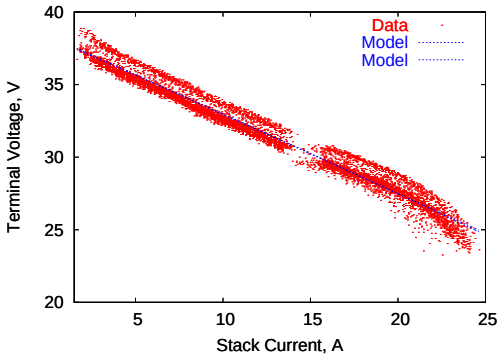

(f) Linear and Quadratic

Figure 6: Measured (dots) and predicted voltage as a function of terminal current using the models in equations (9) in a), (17) in b), (30) in c), (42) in d), and (51) in e) and using the models in equations (61) and (62) in f) for a cross-validation data set.

Table 1 lists parameters and constraints for each model. Each model was identified using its full parameterization and all permutations of a set of constraints. For each model, the first entry in the table is the least constrained choice that provided acceptable cross validation performance and was well-determined. Where applicable, the second entry shows the most constrained model offering comparable performance. Table 1 also lists the Akaike Information Criterion (AIC) model-order selection statistic [28] for each model, relative error and cross-validation relative errors. The relative error in Table 1 is the ratio of the 2-norm of the residual to the 2-norm of the observation. The cross-validation error, "cross-error" in Table 1, is computed in the same way but using the cross validation data set. Fig. 5 shows data and voltage predictions using the models and parameters in Table 1. Cross-validation results, using parameters determined from the data in Fig. 5 to make predictions for a different data set, appear in Fig. 6.

Fuel Cell Handbook Model

Given the constant operating temperature constraint, the parameter μ_4 was set to zero, as the $\mu_4 T$ term is redundant with μ_1 in (9). No further constraints were competitive for this model. Fig. 5(a) shows measured and predicted voltage with respect to stack current for (9) with parameters estimated in row 1 in Table 1. Fig. 6(a) shows cross-validation voltage prediction for (9) with parameters estimated in row 1 in Table 1.

Table 1: Parameter values, AIC and relative error for static fuel cell models.

	Model and Constraint	μ_1	μ_2	μ_3	μ_4	μ_5	μ_6	AIC	error (%)	cross-error (%)
1	Fuel Cell Handbook, (9), $\mu_4 = 0$	3.91e1	-3.45e-1	-2.87e-3	<u>0</u>	2.71e-3	2.46e1	8.82e0	1.75	1.76
2	Kim et al., (17)	3.89e1	-4.56e-1	-6.73e-1	-8.25e-7	6.07e-1		8.81e0	1.74	1.75
3	$\mu_4 = \mu_5 = 0$	3.84e1	-5.40e-1	-5.97e-2	<u>0</u>	<u>0</u>		4.92e0	1.84	1.85
4	Maggio et al., (30), $\mu_4 = 0$	3.92e1	-3.62e-1	-3.11e-3	<u>0</u>	8.77e-5	2.46e1	8.82e0	1.75	1.77
5	$\mu_4 = \mu_5 = 0$, $\mu_6 = 3.00e1$	3.84e1	-5.40e-1	-1.69e-4	<u>0</u>	<u>0</u>	<u>3.00e1</u>	4.92e0	1.84	1.85
6	Amphlett et al., (42), $\mu_2 = \mu_5 = 0$	3.93e1	<u>0</u>	-5.30e-3	-1.12e-1	<u>0</u>	-9.97e-3	6.88e0	1.79	1.81
7	$\mu_2 = \mu_5 = \mu_6 = 0$	3.85e1	<u>0</u>	-2.30e-4	-5.38e-1	<u>0</u>	<u>0</u>	4.92e0	1.84	1.85
8	Chiu et al., (51), $\mu_4 = 0$	3.58e1	-3.27e-1	-1.10e0	<u>0</u>	1.05e0	2.47e1	8.82e0	1.75	1.76
9	$\mu_4 = 0$, $\mu_5 = 0$, $\mu_6 = 2.50e1$	3.84e1	-5.40e-1	-5.97e-2	<u>0</u>	<u>0</u>	<u>2.50e1</u>	4.92e0	1.84	1.85
10	Linear, (61), $\mu_3 = 0$	3.84e1	-5.45e-1	<u>0</u>				2.92e0	1.84	1.85
11	Quadratic, (62), $\mu_3 = \mu_6 = \mu_5 = 0$	3.82e1	-5.17e-1	<u>0</u>	-1.11e-3	<u>0</u>	<u>0</u>	4.92e0	1.83	1.85

Constrained parameter values are underlined. $\mu_7 = 0$ for all models and constraints.

Kim et al. Model

There are no temperature terms in (17), so no modifications were necessary to accomodate the similarity of the temperature response to the load current. To experiment with the importance of the empirical exponential term in (17), μ_4 and μ_5 were constrained to zero in row 3 of Table 1. The parameters are consistent with the unconstrained model, although the error is increased. The AIC score is significantly better than the unconstrained model.

Maggio et al. Model

For modeling (30) at constant PEM operating temperature the parameter μ_4 was constrained to zero, as with the Fuel Cell Handbook model. These two models are very similar, except for the modeling of the diffusion term. Fig. 5(c) and Fig. 6(c) show the predicted voltage with respect to stack current and cross-validation results, respectively. The additional constraints in row 5 discard the diffusion term. The constrained value of μ_6 was selected to avoid inappropriate arguments of the logarithm.

Amphlett et al. Model

At constant temperature, the terms associated with μ_2 and μ_5 in (42) are redundant, and were therefore set to zero. The parameters, AIC and errors are given in row 6. Fig. 5(d) and Fig. 6(d) show the predicted voltage with respect to stack current and cross-validation results, respectively. The constraints in row 7 eliminate the dependence of $R^{internal}$ in (41) on current by setting $\mu_6 = 0$.

Chiu et al. Model

For the model in (51), it proved impossible to avoid numerical problems in the activation term associated with μ_4 during identification without constraining $\mu_4 = 0$. With this constraint and constant temperature, this model becomes equivalent to the Fuel Cell Handbook model. Not surprisingly, the error, cross-validation error, and AIC are the same. In row 9 we eliminate the diffusional term, and the model is exactly equivalent to the Amphlett model as constrained in row 5.

Linear and Quadratic Models

The linear model (61) at constant temperature becomes a simple Thevenin equivalent model by setting the temperature coefficient $\mu_3 = 0$. Parameters and errors are given in row 10. The quadratic model (62) at constant temperature requires eliminating the redundant terms associated with μ_3, μ_5 and μ_6. The parameters, AIC and error are given in row 11.

Dynamic fuel cell model

The voltage E developed over a single cell like Fig. 1 is ideally described by the Nernst equation [11],

$$E = E_0 + \frac{RT}{2F} \ln \frac{P_{H_2} P_{O_2}^{1/2}}{P_{H_2 0}}. \tag{69}$$

Here E_0 is the standard potential of the hydrogen/oxygen reaction (about 1.229 V), R is the universal gas constant, F is Faraday's constant, T is the absolute temperature, and P_{H_2} is the partial pressure of hydrogen available at the anode. In 69 the partial pressures of species appearing on one side of the chemical reaction appear in

the numerator, while the other side of the reaction appears in the denominator. In equilibrium, with no electrical connections, the cell voltage saturates to the standard potential and the ratio of partial pressures is unity. Under load the quantities in the numerator are consumed while quantities in the denominator are produced, and the cell voltage drops.

The relationship between the last term in (69), built-in potentials in the cell, and the current can be modeled by writing the cell voltage as [11]

$$E = E_0 - IR - aT \ln \frac{I}{i_0} - bT \ln \frac{i_L - I}{i_L}. \tag{70}$$

In this equation R is a resistance, including the cell internal resistance, I is the terminal current, and a and b lump terms that can be assumed constant for a particular cell and reaction. Starting from IR, these loss terms are ohmic, the activation overpotential, and the concentration overpotential. Activation overpotential is a loss term associated with energy barriers that must be overcome to start the reaction. Concentration overpotential is a loss associated with the depletion of reactants at high currents. Although the exchange current parameter i_0 for activation and the limiting current i_L for depletion depend on the fuel cell, the activation loss typically dominates the response at low currents, while the effect of the concentration overpotential is most obvious at high currents. The response of our SR-12 PEM stack is nearly linear for a useful range of currents between the activation and concentration regions. Expanding (70) in a Taylor series for currents $I = I_0 + \tilde{I}$ yields

$$\begin{aligned} E &= E_0 - (I_0 + \tilde{I})R - aT \left[\ln \frac{I_0}{i_0} + \frac{1}{I_0} \tilde{I} \right] \\ &- bT \left[\ln \frac{i_L - I_0}{i_L} - \frac{1}{i_L - I_0} \tilde{I} \right] + \text{higher order terms}, \end{aligned} \tag{71}$$

where $\tilde{I}$ is a small signal current and I_0 is the operating point. Assuming that the higher order terms in the current perturbation can be ignored and that $\tilde{I}$ and T are

the variables of interest, then

$$\begin{aligned} E &= (E_0 - I_0 R) - \tilde{I}R - T\left[a \ln \frac{I_0}{i_0} + b \ln \frac{i_L - I_0}{i_L}\right] \\ &- \tilde{I}T\left[\frac{a}{I_0} + \frac{b}{i_L - I_0}\right]. \end{aligned} \tag{72}$$

Writing $T = T_0 + \tilde{T}$, and assuming a stack of n identical cells in series, the stack voltage can be written

$$V(\tilde{I}, \tilde{T}) = A + B\tilde{T} + C\tilde{I} + D\tilde{I}\tilde{T}, \tag{73}$$

where the coefficients in terms of the original parameters are

$$A = n(E_0 - I_0 R) + T_0 B \tag{74}$$

$$B = -n\left[a \ln \frac{I_0}{i_0} + b \ln \frac{i_L - I_0}{i_L}\right] \tag{75}$$

$$C = -nR + T_0 D \tag{76}$$

$$D = -n\left[\frac{a}{I_0} + \frac{b}{i_L - I_0}\right]. \tag{77}$$

Use of $\tilde{T}$ in (73) makes B the sensitivity to temperature change and directly comparable to C, the incremental resistance. The response of a complex system is often dominated by a rate-limiting process or dominant pole that evolves more slowly than others. In a fuel cell, a reasonable dominant pole is the thermal response of the system. We model the thermal response, in absolute temperature, as

$$\alpha \frac{dT}{dt} = -(T - T_{amb}) + \delta I + \gamma I^2 \tag{78}$$

where I is the total current. The temperature T represents a non-specific average internal temperature for purposes of computing the electrical terminal characteristics. The term γI^2 is the contribution of Joule heating to T. The reaction rate is directly proportional to the current I. Thus, δI captures the effects of heat evolved in the reaction, heat lost to bring new reactants to operating temperature, and heat lost

when hot reaction products leave the system. The first term is a simple cooling model incorporating the effect of the constant ambient temperature T_{amb}. This model includes all the effects described in [25]. To combine (73) with (78), the thermal model must be expressed in terms of $\tilde{T}$, where $T = T_0 + \tilde{T}$ and $\tilde{T}$ is the small signal temperature change. Substituting in (78) yields

$$\begin{aligned} \alpha \frac{d(T_0 + \tilde{T})}{dt} &= -(T_0 + \tilde{T} - T_{amb}) + \delta(I_0 + \tilde{I}) \\ &+ \gamma(I_0 + \tilde{I})^2. \end{aligned} \tag{79}$$

If T_0 is set to the equilibrium temperature of the system at the linearization current I_0, then

$$\alpha \frac{dT_0}{dt} = -(T_0 - T_{amb}) + \delta I_0 + \gamma I_0^2 = 0 \tag{80}$$

With this definition, $\tilde{T}$ has the interpretation as the perturbation in temperature due to $\tilde{I}$. Subtracting yields

$$\alpha \frac{d\tilde{T}}{dt} = -\tilde{T} + (2\gamma I_0 + \delta)\tilde{I} + \gamma \tilde{I}^2. \tag{81}$$

Rewriting with $\beta = 2\gamma I_0 + \delta$,

$$\alpha \frac{d\tilde{T}}{dt} = -\tilde{T} + \beta \tilde{I} + \gamma \tilde{I}^2, \tag{82}$$

The parameters α, β and γ in (82) are independent.

If measurements of $\tilde{I}$, $\tilde{T}$ are available, then the relationship between $\tilde{I}$ and $\tilde{T}$ measurements can be used to estimate the parameters of the thermal system in (82). Similarly, $\tilde{I}$, $\tilde{T}$, and V measurements support the parameters of the electrical system in (73). Therefore, the combined set of parameters to estimate when thermal and electrical information is available consists of A, B, C, D, α, β, γ. However, if measurements of $\tilde{I}$ and V are available, then the system is over-parameterized. Equation (82) is a linear differential equation. If both β and γ are scaled, a scaled internal

version of $\tilde{T}$ will appear in the model. However, every occurrence of $\tilde{T}$ in (73) is multiplied by a parameter that can be adjusted to accommodate any scaling of $\tilde{T}$, so this would have no impact on the quality of the voltage prediction. The practical consequence is that the model can only be expected to predict something proportional to $\tilde{T}$ with parameters determined by $\tilde{I}$ and V measurements. This is not a big limitation, because in practice the actual $\tilde{T}$ is difficult to measure. However, it is often convenient to measure temperature changes somewhere on the thermal gradient between T and T_{amb} that are proportional to $\tilde{T}$.

Experimental setup for validation of dynamic fuel cell model

The SR-12 was allowed to complete its factory programmed warm-up procedure and was then operated for 30 minutes under a 2 A load before testing. The purpose of this procedure was to obtain repeatable initial operating temperature in the system. Temperatures at the measurement locations equilibrated roughly an order of magnitude faster than the warmup interval. A number of dynamic data sets containing voltage, current and temperature profiles were recorded.

Validation results for dynamic model

The thermal model in (82) was considered first, using measurements of $\tilde{I}$ and $\tilde{T}$ to support the parameters α, β and γ. Parameters were estimated using the Levenburg-Marquardt method [27] to minimize the least-square error criterion for the temperature prediction. Parameters are given in the first row of Table 2, and a comparison of the measured and predicted thermal response appears in Fig. 7. Rows two and three of Table 2 explore the effect of eliminating terms in the thermal model.

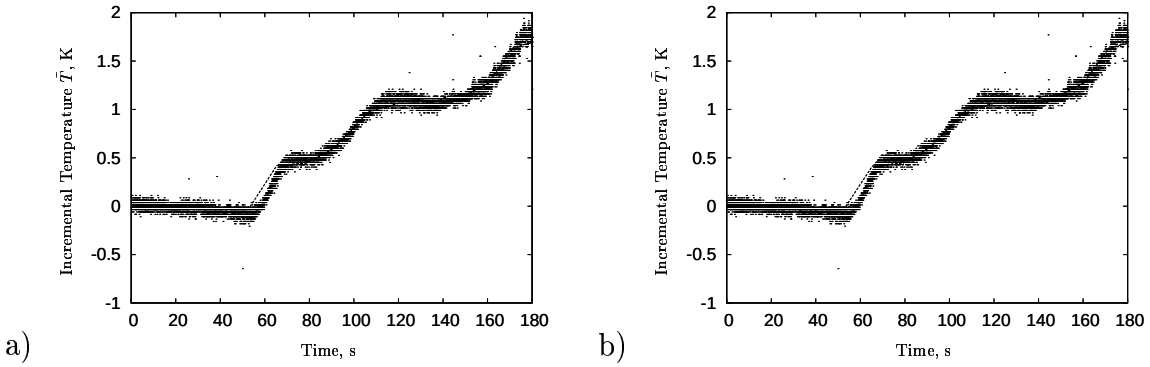

Figure 7: Measured (dots) and predicted temperature using the model in (82). Performance with the constraint $\beta = 0$ is shown in 7.b. The current waveform used for these graphs appears in Fig. 9.d.

The performance of these constrained, simpler models can be judged by the relative values of the Akaike information criterion (AIC). The AIC statistic [28] attempts to balance quality of fit and model complexity by increasing with the number of parameters and decreasing for smaller residual variance. Ideally the AIC attains a minimum for the "correct" compromise between number of parameters and model performance. For the thermal models, the AIC of (82) is close to the value attained with the constraint $\beta = 0$. The similar performance of these two models is highlighted in Fig. 7, where the constrained thermal model appears in the lower graph. The AIC for the cross validation dataset is similar for both models.

The static voltage equation in (73) was fit using $\tilde{I}$ current data and $\tilde{T}$ temperature data to predict the observed voltage. Rows four through six of Table 1 show parameters for (73), with and without constraints. The constraint $B = 0$, which effectively eliminates a first-order temperature dependence, produced AIC scores similar to the full model. However, the AIC for the cross validation data set favors (73) without constraints. Fig. 8.a shows measured and predicted voltage for voltage model without constraints, while Fig. 8.b shows the model performance with the constraint $B = 0$.

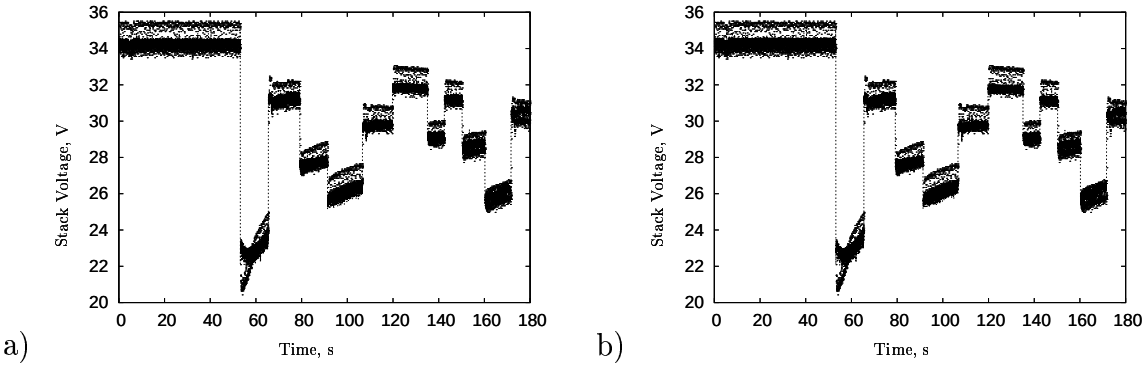

Figure 8: Measured (dots) and predicted voltage using the model in (73). Data in 8.b show model performance with the constraint $B = 0$. The measured temperature and current used for these graphs appear in Fig. 9.c and Fig. 9.d, respectively.

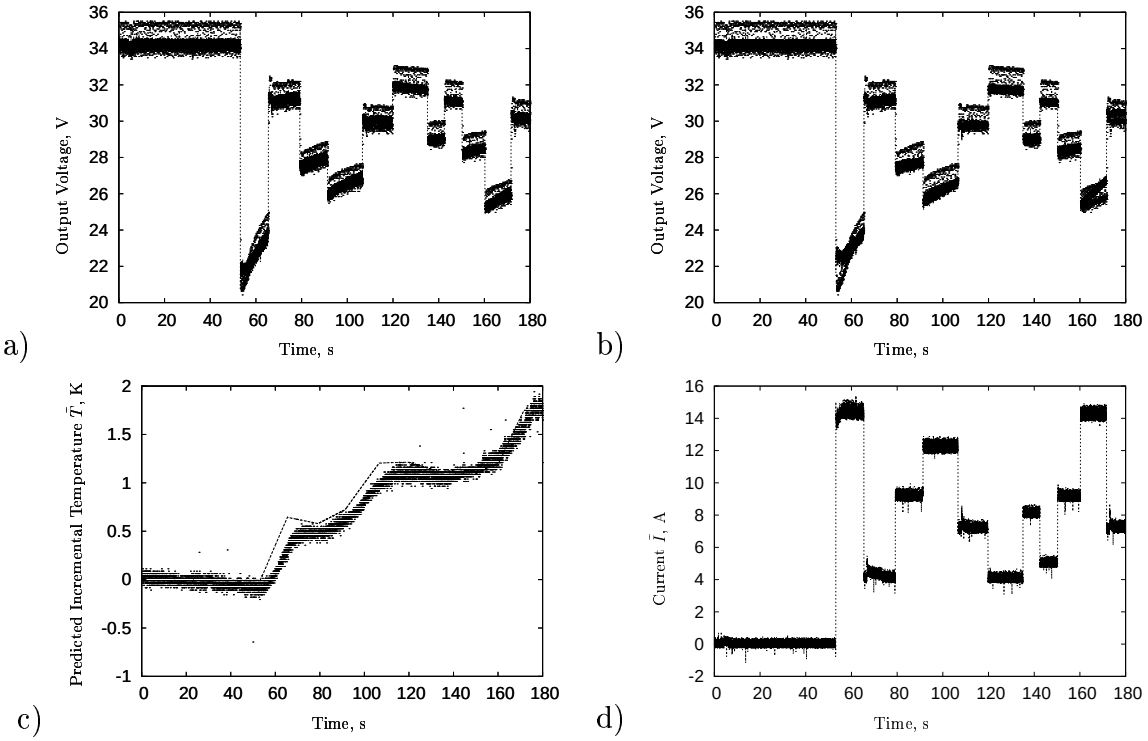

Figure 9: Measured (dots) and predicted voltage using (82) and (73) appear in 9.a and 9.b. The constraint $B = 0$ was used for 9.b. 9.c shows the measured temperature and internal incremental temperature prediction for the constraint model with $B = 0$. The associated measured current waveform appears in 9.d.

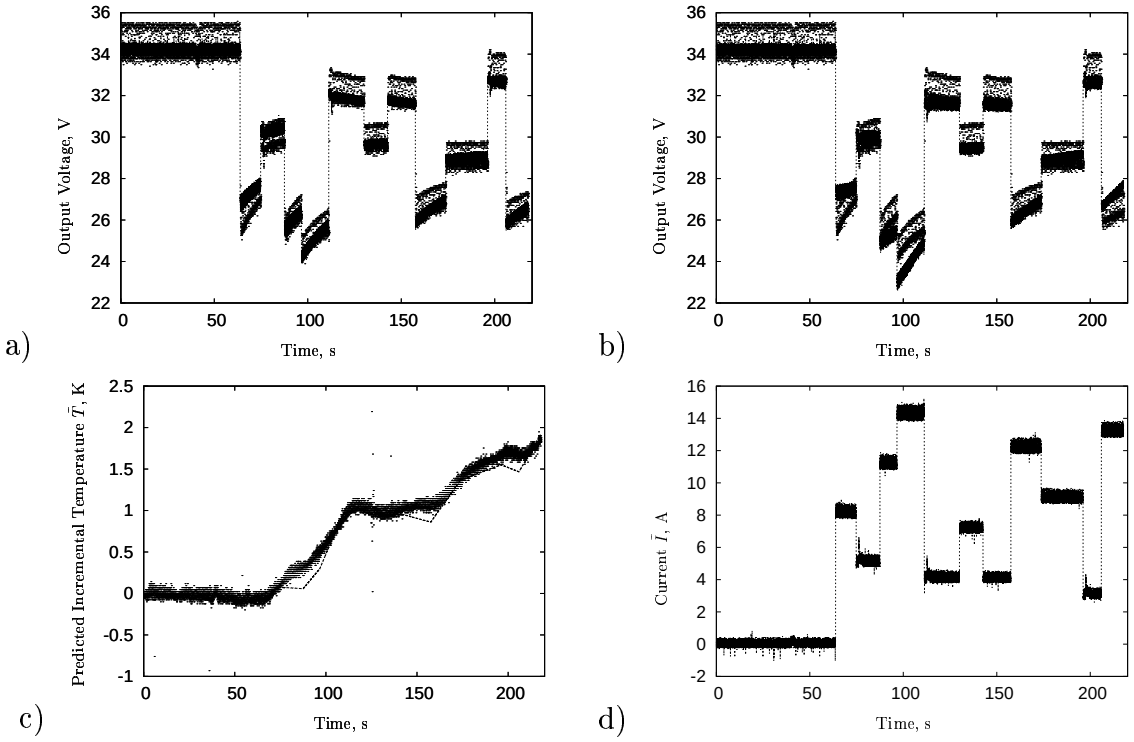

Figure 10: Measured (dots) and predicted voltage using (82) and (73) are shown in 10.a and 10.b for a cross-validation data set. The constraint model with $B = 0$ was used for 10.b. 10.c shows the measured temperature and internal incremental temperature prediction for the constraint model with $B = 0$. The associated measured current waveform appears in 10.d. The model parameters used for these plots were determined using the data in Fig. 9.

Temperature and current measurements used for the models in Fig. 8 are plotted in Fig. 9.c and Fig. 9.d, respectively. Combinations of constraints that do not appear in Table 2 were not competitive.

The combination of (73) and (82) was fit using just the electrical terminal measurements $\tilde{I}$ and V, minimizing the least square criterion for voltage predictions. Four combinations of constraints for (73) and (82) were considered, as in Table 2 rows 7-10, motivated by the success of these constraints in the previous two modeling stages. Fig. 9.a shows a comparison of measured and predicted voltage for the model

Table 2: Parameter values and Akaike information criterion (AIC) for dynamic fuel cell models using (82) and (73).

	Model and Constraint	α	β	γ	A	B	C	D	AIC	Cross AIC
		s	KA^{-1}	KA^{-2}	V	VK^{-1}	VA^{-1}	$VA^{-1}K^{-1}$		
1	Eqn (82)	6.41e2	-1.40e-1	1.21e-1					-5.496	-4.941
2	$\beta = 0$	4.97e2	<u>0</u>	8.55e-2					-5.494	-5.020
3	$\gamma = 0$	1.60e2	3.41e-1	<u>0</u>					-5.273	-5.281
4	Eqn (73)				3.44e1	1.68e-1	-8.09e-1	1.43e-1	-0.967	-0.733
5	$B = 0$				3.44e1	<u>0</u>	-8.12e-1	1.60e-1	-0.961	-0.702
6	$D = 0$				3.42e1	1.14e0	-7.56e-1	<u>0</u>	-0.692	-0.578
7	Eqn (82), (73)	2.90e1	1.80e0	-2.63e-2	3.43e1	2.36e-2	-9.08e-1	2.20e-2	-1.192	-1.035
8	$B = 0$	2.88e2	-7.16e-1	1.27e-1	3.43e1	<u>0</u>	-8.43e-1	1.80e-1	-1.024	-0.622
9	$\beta = 0$, $\gamma = 8.55e-2$	5.39e2	<u>0</u>	<u>8.55e-2</u>	3.43e1	8.40e-2	-8.04e-1	1.61e-1	-0.913	-0.612
10	$\beta = 0$, $\gamma = 8.55e-2$, $B = 0$	5.45e2	<u>0</u>	<u>8.55e-2</u>	3.44e1	<u>0</u>	-8.05e-1	1.63e-1	-0.908	-0.607

Constrained parameter values are underlined.

without constraints, using the current waveform in Fig. 9.d. The high-frequency variation in measured voltage is due to the unique cell-shorting operating characteristic of the SR-12. The voltage prediction for the next most competitive model (row 8 of Table 2) appears in Fig. 9.b. The parameters for the constrained models in rows 8-10 of Table 2 are quite consistent, and these models produced similar predictions of the internal temperature perturbation $\tilde{T}$. Fig. 9.c shows the internal temperature prediction for model 8 in Table 2. Note that the model temperature *leads* the measured temperature by a few seconds. This is physically reasonable, as the membrane temperature probably leads the temperature at the measurement site, which is separated from the membrane by about 3mm of gas diffusion material. Models 9 and 10 in Table 2 constrain γ with β to avoid over-parameterization when combining (73) and (82). The unconstrained model does not predict internal temperature perturbations, the parameters are not consistent with the constrained models, but the AIC is significantly better. The quality of fit for the unconstrained model in Fig. 9.a appears superior even to the model in Fig. 8, which is supported by actual temperature measurements. Fig. 10 shows cross-validation results. Voltage predictions for the unconstrained model are given in Fig. 10.a, while Fig. 10.b shows cross validation results for the best constrained model with $B = 0$. Fig. 10.c shows cross validation temperature predictions for the constrained model. The cross-validation current waveform appears in Fig. 10.d.

Fuel cell modeling results

The quality of fit for all the static models is relatively good. The lowest (best) AIC score is achieved by the linear Thevenin equivalent model, primarily because it has only two parameters. On the other hand, the linear model in row 10 of Table 1

provides performance that is essentially equivalent to the more complicated models, including the quadratic and the constrained models in rows 3, 5, 7, and 9. There is little reason to consider models that perform as well as the linear model, but are more complex. The performance of the minimally constrained models in rows 1, 2, 4, 5, and 8 is very close, even in cross-validation.

The dynamic modeling results in Table 2 suggest that for modeling temperature from current (rows 1-3) and voltage from temperature and current (rows 4-6), the full set of parameters for (82) or (73) is unnecessary. For modeling voltage as a function of current, the quality of fit for voltage predictions given temperature measurements suggests temperature as a reasonable state variable for our stack. However, the model combining (82) and (73) provides some surprising results. The constraint $B = 0$ appears to cause the combined model to predict the internal temperature, even though temperature is not part of the error criterion. However, the constrained models do not cross-validate as well as the unconstrained model. In addition, the internal state $\tilde{T}$ of the unconstrained model does not resemble the measured temperature. The state in the unconstrained model may capture some phenomena other than or in addition to temperature. It is likely because temperature, humidity, and several other physical quantities are tightly linked in PEM fuel cells.

PEM FUEL CELL DEGRADATION SETUP

The degradation setup presented in this section was used to obtain data that supports the degradation modeling approach. The setup allows continuous monitoring of PEM fuel cell membranes under transient-rich load waveform. The setup consists of 80 membranes per test system. This setup provides a record of voltage, current, and temperature profiles for each membrane over its entire life span.

Degradation setup

Fig. 11 shows overall block diagram of the PEM fuel cell degradation monitoring setup. Various parts of the the entire setup are discussed in the following sub-sections.

Fuel cell membrane test system

The Avista Independence 1000, a commercially available 1000 W PEM fuel cell system, was selected for the membrane test system. The Independence 1000 (See Fig. 13) is a modular system consisting of eight hot-swappable PEM fuel cell cartridges. Each cartridge has electrical and gas connections for ten membrane-electrode assemblies. This hot swap capability increases system reliability, because failed cartridges can be replaced in the field. For PEM degradation experiments, the hot-swap feature also allows removal of cartridges without disturbing the other membranes under test.

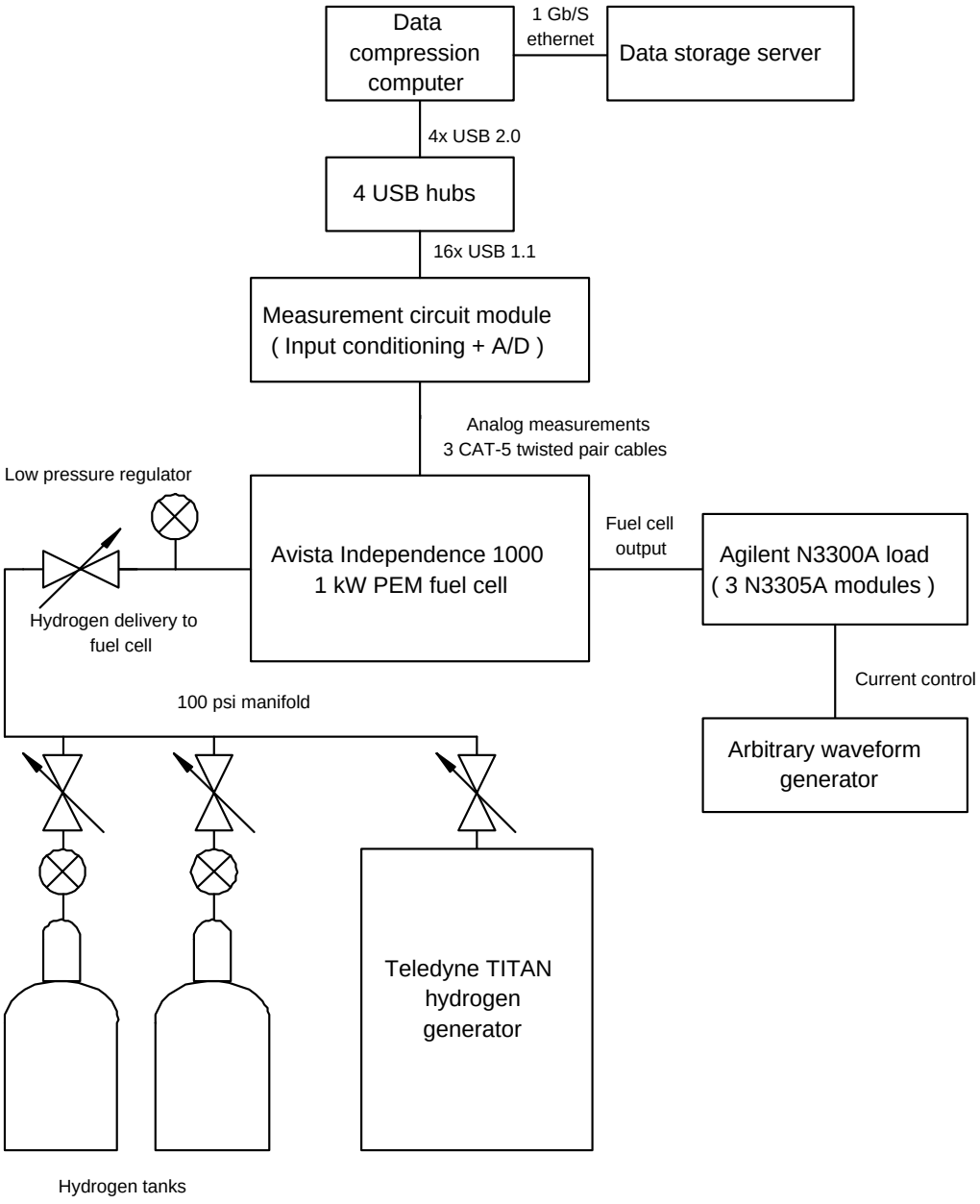

Figure 11: Schematic diagram of PEM membrane degradation monitoring system.

Figure 12: PEM membrane degradation monitoring system.

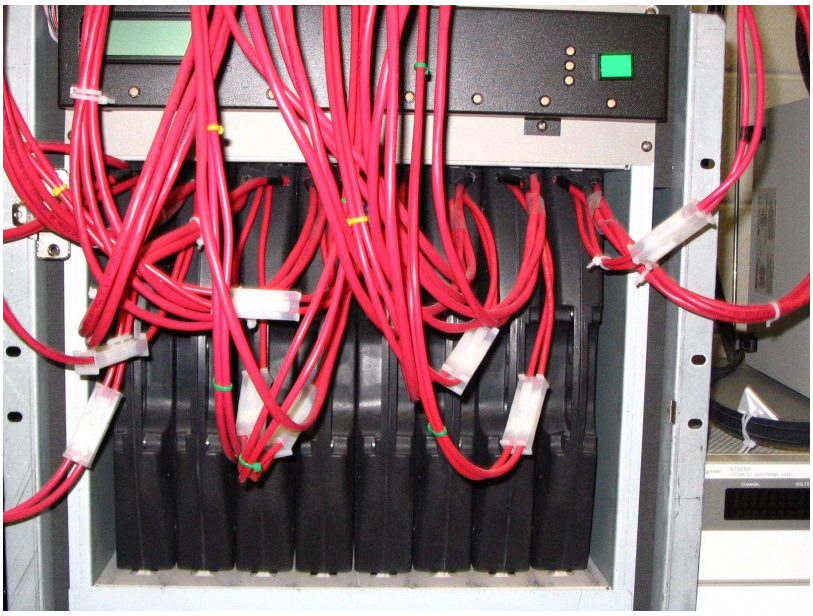

Figure 13: Fuel cell membrane test system, Avista Independence 1000. The modular system consists of eight fuel cell cartridges.

Fuel cell cartridge modifications and measurement circuit module

Each of the eight PEM fuel cell cartridges contain ten membranes in series. The ten cells are arranged such that there are five cells on each side of the cartridge, Fig. 14. For each side of the cartridge, it is necessary to measure five differential voltages across the cell membranes, one current, and a heat-sink temperature measurement. The current mesurements for each side of the cartridge should be the same, as the cells are in series.

For each cartridge there is a corresponding circuit module as shown in Fig. 15. Each circuit module consists of custom analog input conditioning board and two custom analog to digital conversion boards for each side of the cartridge. Each circuit module is connected to the PEM cartridge by a set of three CAT-5 twisted pair cables, using standard CAT-5 connectors. The eight circuit modules needed for an Independence 1000 test stand are mounted on an aluminum panel that slides into a standard card rack. The circuit modules are designed to be easily interchangeable in the event of failure.

The input conditioning board is connected to two custom A/D boards used to acquire the required measurements from the two sides of each cartridge. Each A/D card captures the common series current, five differential membrane potentials, and the heat-sink temperature for each side. Figure 14 shows the modifications made to each cartridge to obtain the desired measurements. The series current of the cells is measured with an LEM LA-150 closed-loop Hall effect sensor mounted on the the input conditioning board. Membrane potential is monitored by a set of twisted-pair sense wires soldered to the current collecting plates on the PEM cartridge. The membrane potentials are isolated using an Analog Devices AD628 differential instrumentation amplifier in the pre-processing circuitry. Temperature is measured

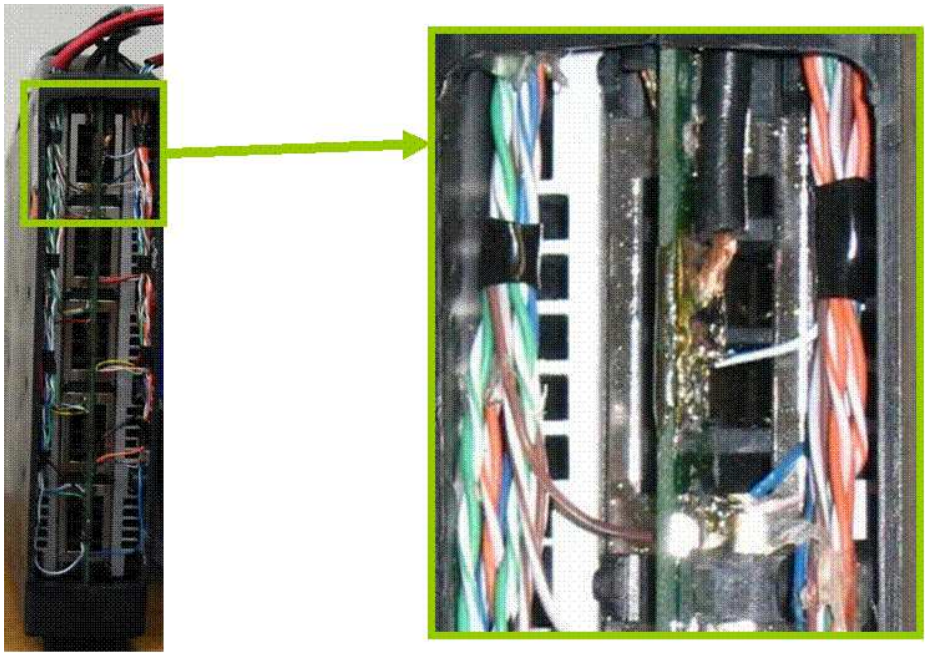

Figure 14: Cartridge modifications to enable measurement of differential voltages, heat-sink temperature and current for each side of the cartridge.

as a voltage from an Avista-installed LM35 temperature sensor glued to the heatsink in the cartridge. All 112 measurement channels are sampled at 2040.8 Hz with 14-bit resolution. Each A/D card is connected to a USB hub with four input port through USB 1.1 cable. The data compression computer collects the data from the USB hubs and saves data in the form of compressed files on the data storage server.

Transient load

To capture practical field conditions, a transient-rich load is used in the degradation setup. The Avista Independence 1000 is connected to an Agilent active load, N3300A, featuring a 10kHz bandwidth. Labview software was used to program a

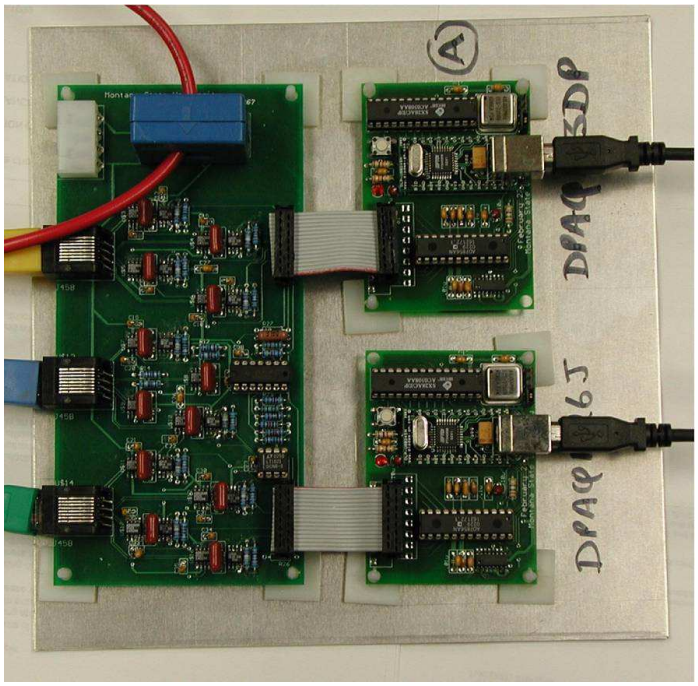

Figure 15: Custom analog input conditioning board and two analog to digital conversion boards for each side of cartridge. The analog processing board on the left receives the measurements from cartridge and the boards on the right digitize the information and send it through USB to the storage server.

National Instruments arbitrary wave generator, for the external analog programming provision of the Agilent active load. This input signal makes the Agilent electronic load act like transient loads for the fuel cells. For example, fuel cells are being tested for the real transients collected from the operation of lathe, vacuum, etc.

Hydrogen generator

The PEM degradation setup requires a continous, reliable and safe supply of hydrogen. A Teledyne TITAN hydrogen generator is installed as shown in Fig. 12 in the degradation setup that provides up to 20 standard litres per minute (slpm). Fig. 16 shows a schematic of the hydrogen generator setup. The generator consists of electrolysis module subsystem, feedwater subsystem, gas control subsystem, and programmable controller. The system has built-in shutdown alarms for some critical situations, for example, high gas pressure, low electrolyte level. The generator maintains a nominal manifold pressure of about 100 psi. Hydrogen is delivered to the fuel cells via three individually regulated output lines. Two back-up hydrogen tanks are provided in case transient demand is in excess of 20 slpm or the hydrogen generator needs maintainence.

A Culligan water purification system is installed to provide the generator with feedwater of minimum allowable electrical resistivity of 200 kΩ. The programmable controller in the hydrogen generator shuts off the generator in case the water purity drops below the required value. Safety sensors including a hydrogen leak detector and Dwyer differential pressure gauge for the vent hood are installed to shut off the hydrogen generator in any hazardous situation. For example, if the room exhaust vacuum drops below a preset level, the hydrogen generator shuts off.

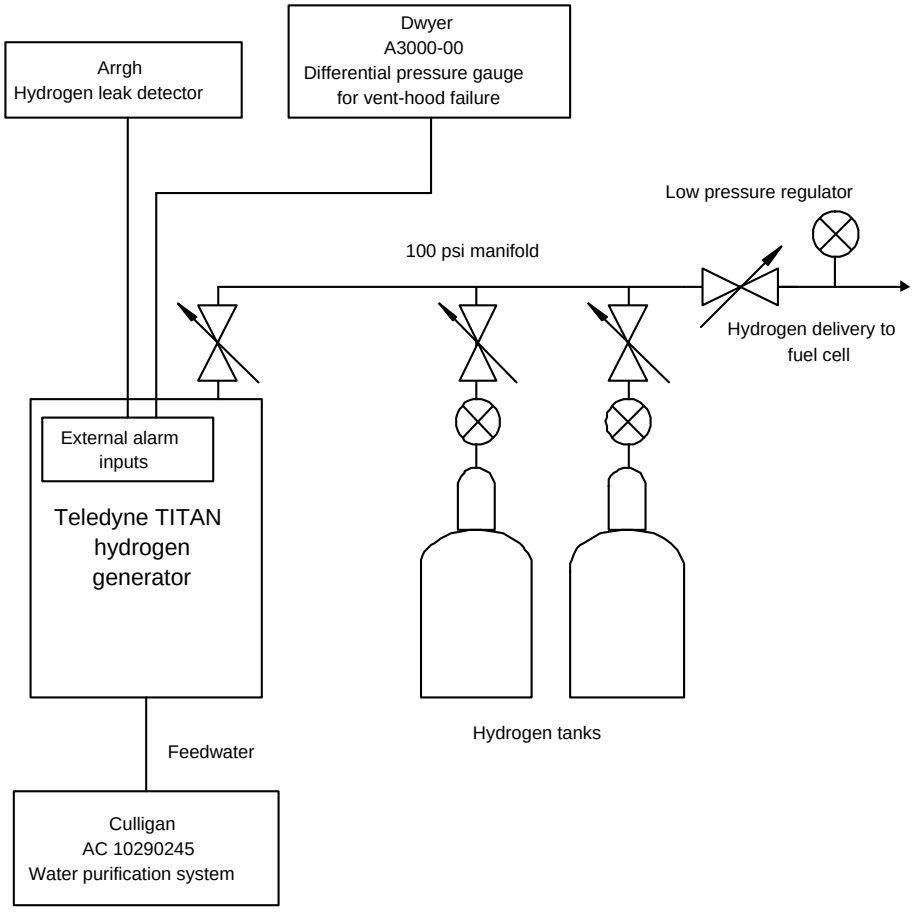

Figure 16: Schematic of hydrogen generation set-up.

PEM FUEL CELL DEGRADATION MODELING AND RESULTS

The data for each membrane is collected and stored with a name tag containing corresponding cartridge number and time of data collection. The data storage server registers the performance history of each cartridge. In an event of cartridge failure, a new cartridge is installed and data-collection process is resumed.

Modeling of PEM fuel cell degradation

In the previous fuel cell modeling chapter, various physical phenomena in the PEM fuel cell are related to the electrical terminal measurements. The parameters derived in each model are associated with some distinct physical process inside the fuel cell. Therefore, it is anticipated to capture the fuel cell membrane degradation by observing change in parameters over a period of time.

The data obtained for a new membrane can be used to fit many different models. For example, Fig. 17(a) shows the current recorded for a membrane in new condition. There is a change in persistence of individual membrane excitation with degradation. Fig. 17(b) shows the current profile of the same membrane after degradation. A simple model is needed that can be supported both with new membrane data and degraded membrane data.

Row 10 of Table 1 and row 5 of Table 2 show that simple linear resistive model is comparable to other complex models. Therefore, similar to equation (61) and (73), simple linear resistive model to study degradation can be written as

$$V_{cell} = \mu_1 - \mu_2 \tilde{I} \tag{83}$$

where μ's are the identification parameters. $\tilde{I}$ and V_{cell} are small signal current

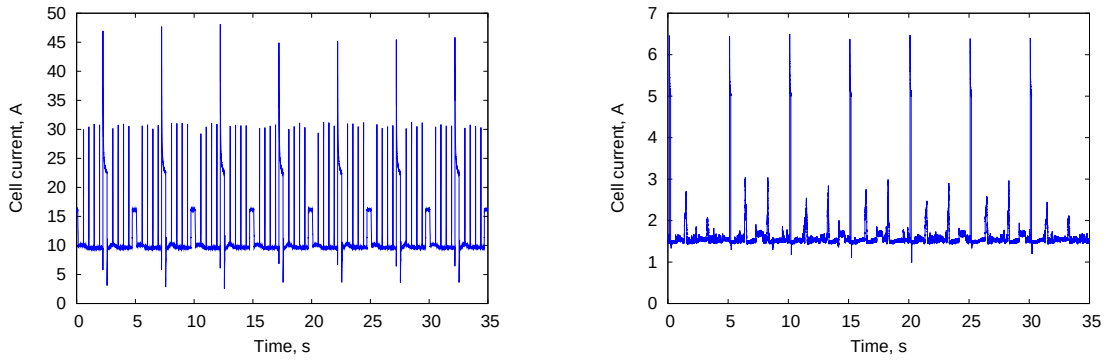

(a) Un-degraded state

(b) Degraded state

Figure 17: Observed current data for a membrane during un-degraded and degraded states.

flowing though the fuel cell and voltage across the cell membrane. The identification parameters, μ_1 and μ_2 are considered as open circuit voltage and resistance for each fuel cell membrane, respectively.

Average power is monitored over the life span of the membrane under transient load conditions. The variation of parameters in contrast with the change in observed power is used to characterize PEM membrane degradation or failure.

Degradation results

The linear resistive model in (83) was considered, using measurements of $\tilde{I}$ and V for each membrane to support the parameters μ_1 and μ_2. Parameters were estimated for membranes using the Levenburg-Marquardt method [27] to minimize the least-square error criterion for the voltage prediction and trends in parameters variations for a number of days were observed. After examining the drift in the parameters values and corresponding fluctuations in power, some interesting observations were made. The following two membrane degradation or failure modes were identified.

Decreasing voltage, increasing resistance failure mode

The open circuit voltage, μ_1 starts decreasing and internal membrane resistance, μ_2 starts increasing for the membranes that degrade in this manner. Fig. 18 shows life span power performance for a set of four membranes in series that failed in this mode. Fig. 19-Fig. 22 present the time plot of corresponding open circuit voltage and internal resistance for the membranes given in Fig. 18.

For Fig. 18, the membranes started degrading from the second experiment run day with a decline in the observed average power and there is a gradual increase in resistance and decrease in voltage from this point onwards. For example, for the membrane given in Fig. 18(b), the open circuit voltage (See Fig. 20(a)) has reduced by a factor of 8 and internal membrane resistance (See Fig. 20(b)) has increased by factor of 15, approximately, from the point it started degrading to complete failure.

Similarily, Fig. 23-Fig. 27 explore another set of four membranes in series that failed in a similar fashion.

Increasing resistance failure mode

The open circuit voltage, μ_1 remains in a range and internal membrane resistance, μ_2 starts increasing for the membranes that degrade in this manner. Fig. 28 shows life span power performance for a set of four membranes in series that failed in this mode. Fig. 29-Fig. 32 present the time plot of corresponding open circuit voltage and internal resistance for the membranes given in Fig. 28.

For Fig. 28, the membranes started degrading from the sixth experiment run day with a decline in the observed average power and there is a gradual increase in resistance from this point onwards. The open circuit voltage did not reduce as observed in

the previous mode. For example, for the membrane given in Fig. 28(d), the internal membrane resistance (See Fig. 32(b)) has increased by factor of 13, approximately, from the point it started degrading to complete failure.

Similarily, Fig. 33-Fig. 37 explore another set of four membranes in series that failed in a similar fashion.

The cell voltage in (83) was fit using $\tilde{I}$ current data, minimizing the least square criterion for voltage predictions. The measured and predicted voltage as a function of current for the membrane given in Fig. 28(a), before and after sixth experiment run day are given in Fig. 38 and Fig. 39, respectively. Fig. 38 and Fig. 39 show that the linear resistive model perform well with decent individual membrane excitation.

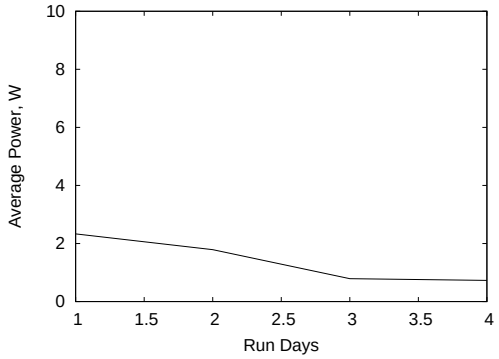

(a) Average Power for membrane 1

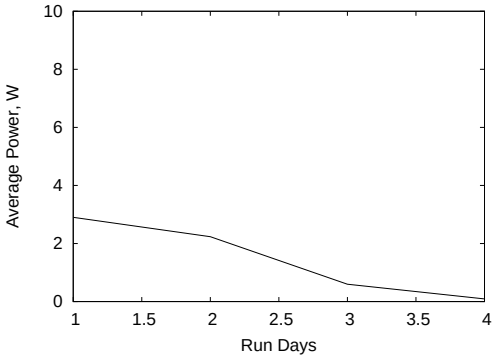

(b) Average Power for membrane 2

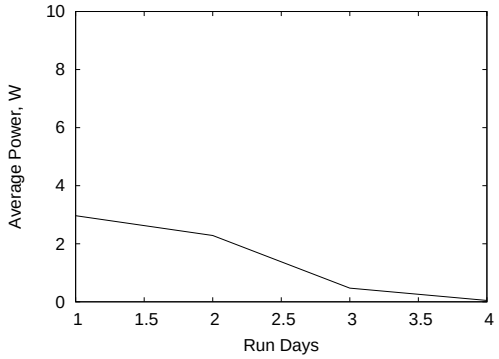

(c) Average Power for membrane 3

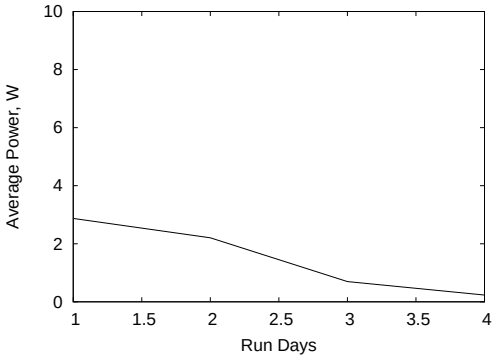

(d) Average Power for membrane 4

Figure 18: Average power for first set of four membranes in series as a function of experiment run days.

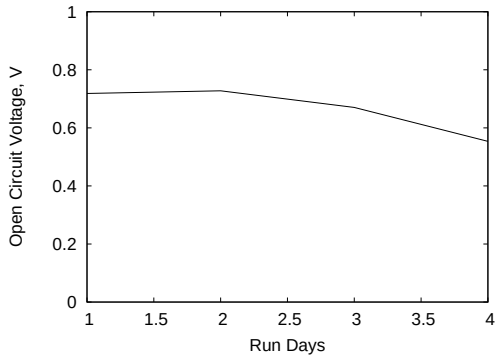

(a) Open Circuit Voltage, μ_1

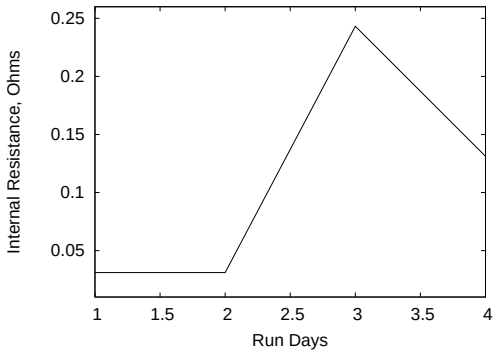

(b) Internal Resistance, μ_2

Figure 19: Parameters, μ_1 and μ_2, of equation (83) for the membrane given in Fig. 18(a) as a function of experiment run days.

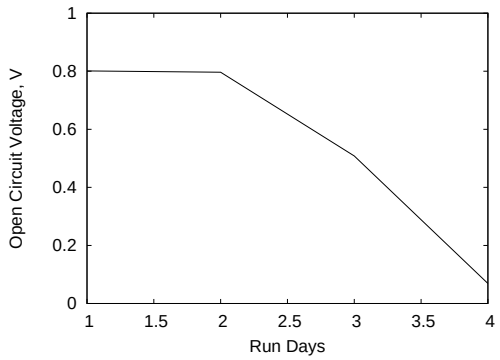

(a) Open Circuit Voltage, μ_1

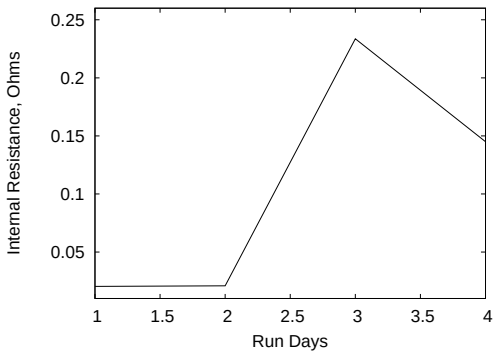

(b) Internal Resistance, μ_2

Figure 20: Parameters, μ_1 and μ_2, of equation (83) for the membrane given in Fig. 18(b) as a function of experiment run days.

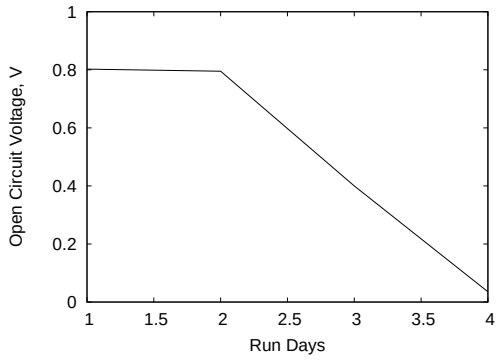

(a) Open Circuit Voltage, μ_1

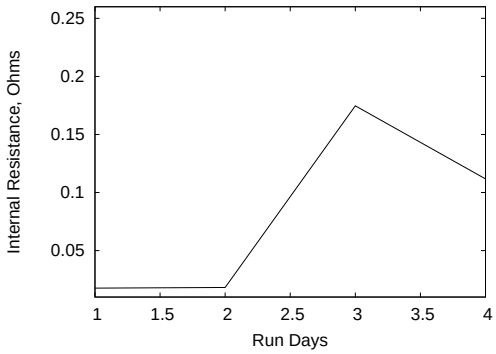

(b) Internal Resistance, μ_2

Figure 21: Parameters, μ_1 and μ_2, of equation (83) for the membrane given in Fig. 18(c) as a function of experiment run days.

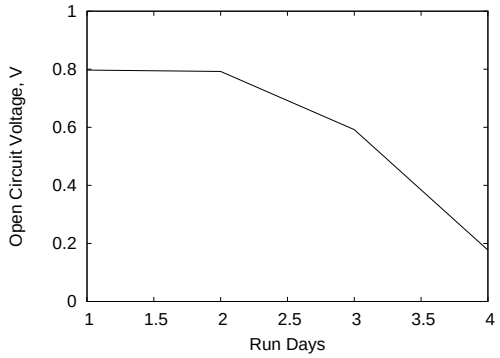

(a) Open Circuit Voltage, μ_1

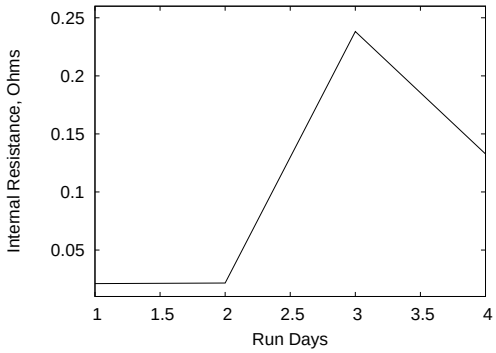

(b) Internal Resistance, μ_2

Figure 22: Parameters, μ_1 and μ_2, of equation (83) for the membrane given in Fig. 18(d) as a function of experiment run days.

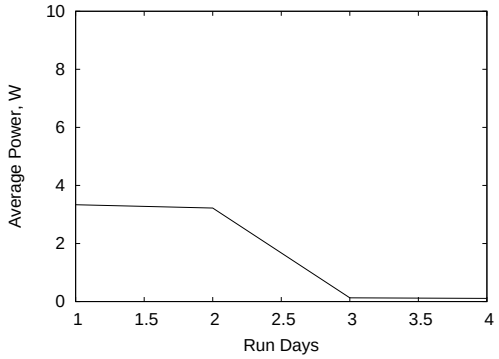

(a) Average Power for membrane 1

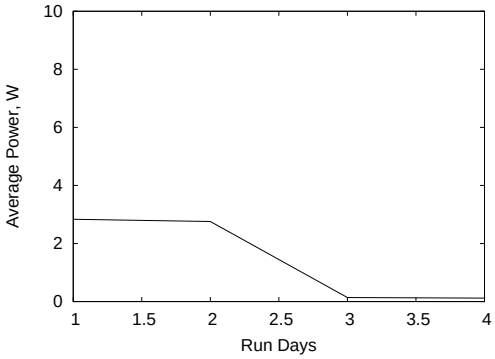

(b) Average Power for membrane 2

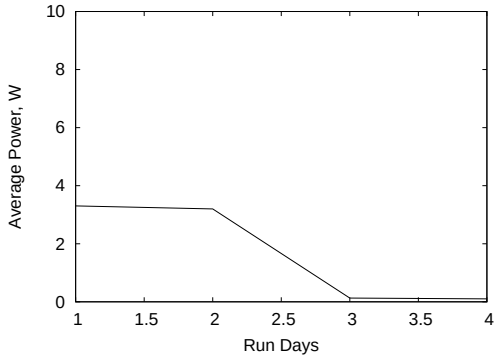

(c) Average Power for membrane 3

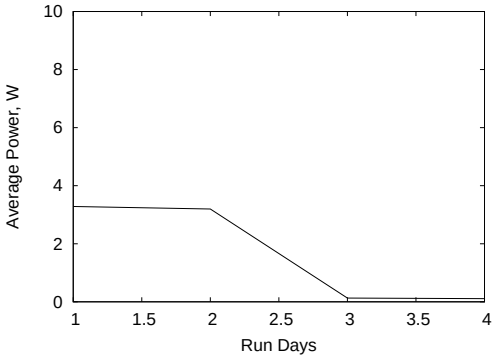

(d) Average Power for membrane 4

Figure 23: Average power for second set of four membranes in series as a function of experiment run days.

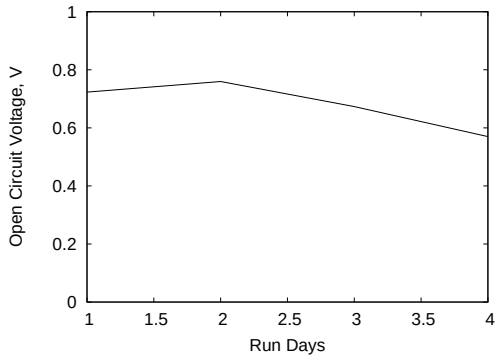

(a) Open Circuit Voltage, μ_1

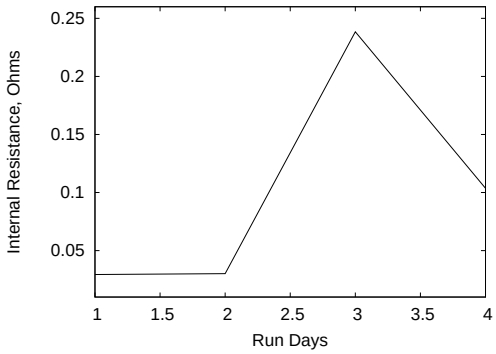

(b) Internal Resistance, μ_2

Figure 24: Parameters, μ_1 and μ_2, of equation (83) for the membrane given in Fig. 23(a) as a function of experiment run days.

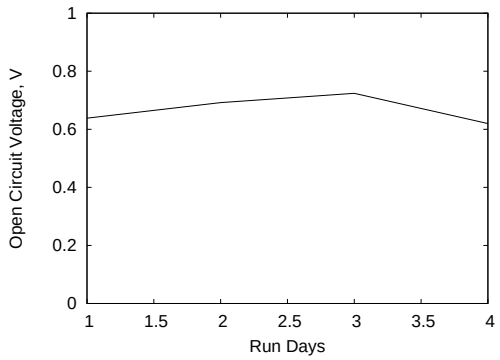

(a) Open Circuit Voltage, μ_1

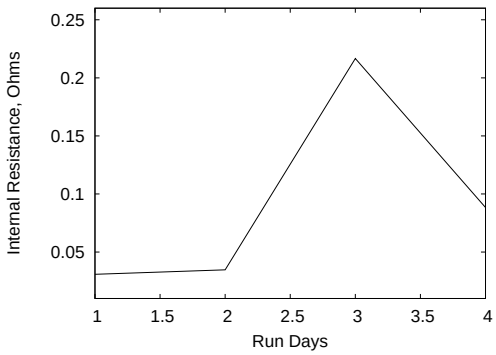

(b) Internal Resistance, μ_2

Figure 25: Parameters, μ_1 and μ_2, of equation (83) for the membrane given in Fig. 23(b) as a function of experiment run days.

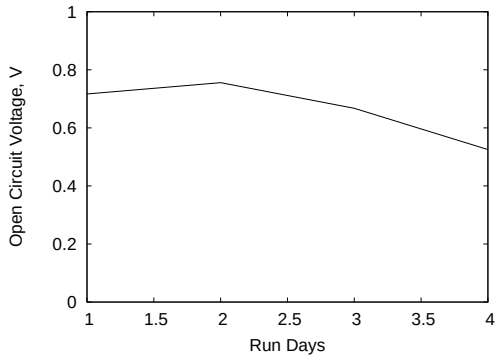

(a) Open Circuit Voltage, μ_1

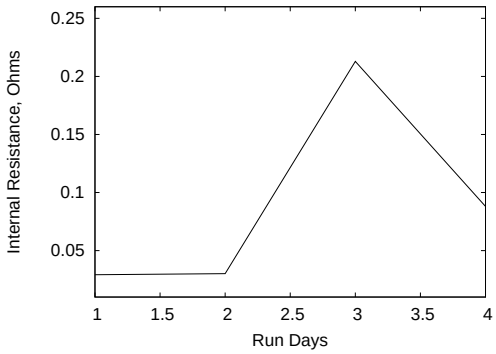

(b) Internal Resistance, μ_2

Figure 26: Parameters, μ_1 and μ_2, of equation (83) for the membrane given in Fig. 23(c) as a function of experiment run days.

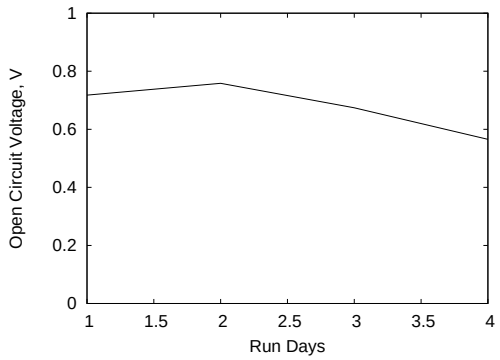

(a) Open Circuit Voltage, μ_1

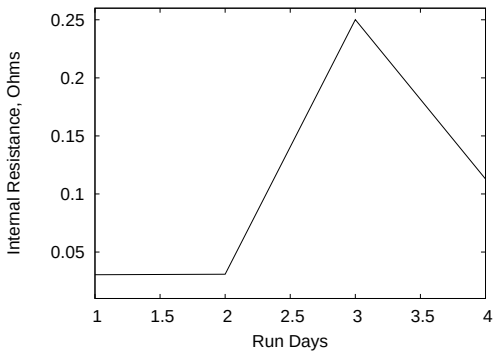

(b) Internal Resistance, μ_2

Figure 27: Parameters, μ_1 and μ_2, of equation (83) for the membrane given in Fig. 23(d) as a function of experiment run days.

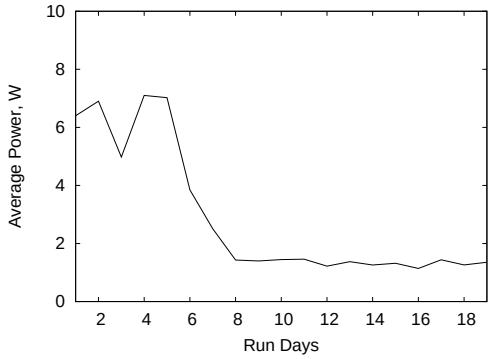

(a) Average Power for membrane 1

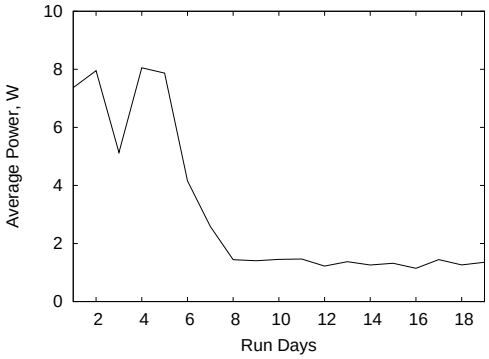

(b) Average Power for membrane 2

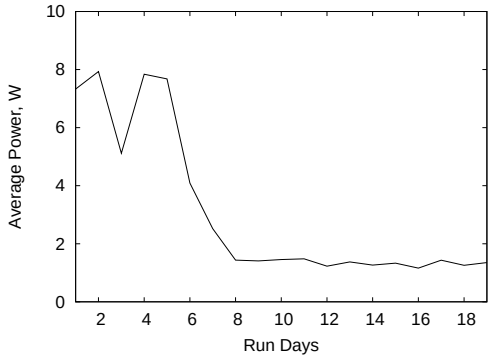

(c) Average Power for membrane 3

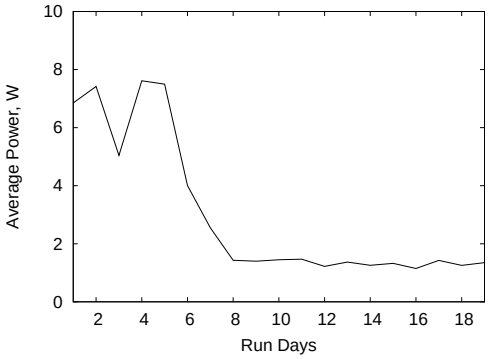

(d) Average Power for membrane 4

Figure 28: Average power for third set of four membranes in series as a function of experiment run days.

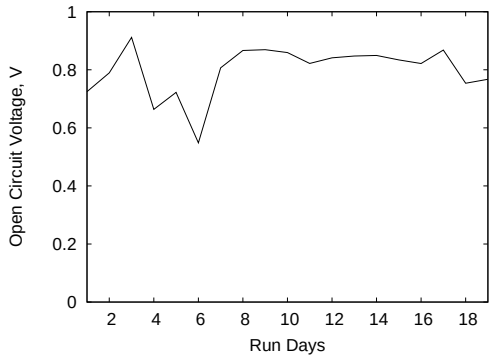

(a) Open Circuit Voltage, μ_1

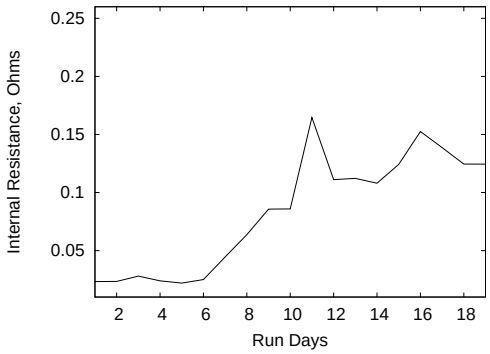

(b) Internal Resistance, μ_2

Figure 29: Parameters, μ_1 and μ_2, of equation (83) for the membrane given in Fig. 28(a) as a function of experiment run days.

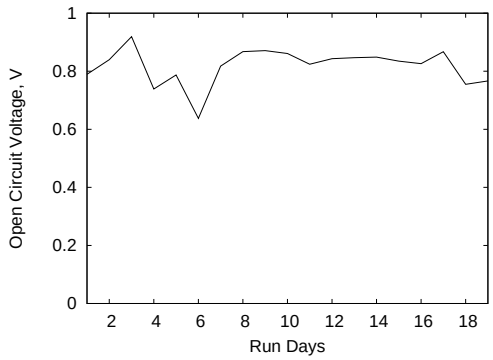

(a) Open Circuit Voltage, μ_1

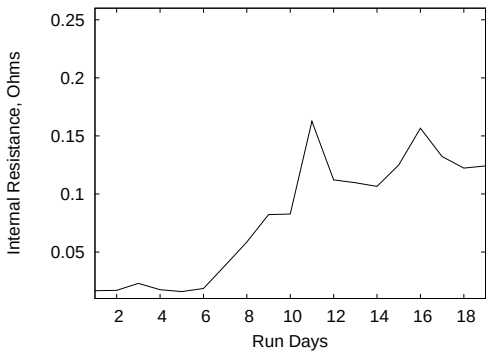

(b) Internal Resistance, μ_2

Figure 30: Parameters, μ_1 and μ_2, of equation (83) for the membrane given in Fig. 28(b) as a function of experiment run days.

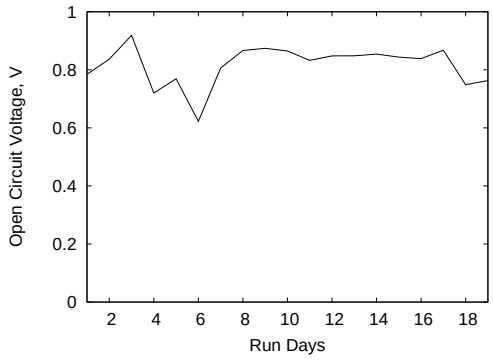

(a) Open Circuit Voltage, μ_1

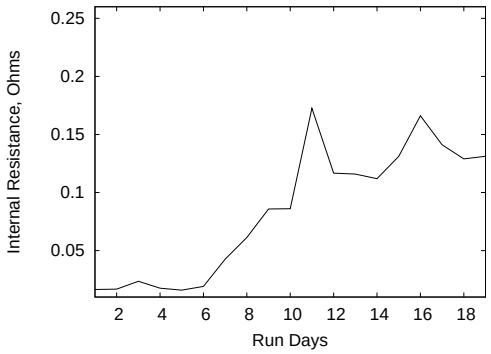

(b) Internal Resistance, μ_2

Figure 31: Parameters, μ_1 and μ_2, of equation (83) for the membrane given in Fig. 28(c) as a function of experiment run days.

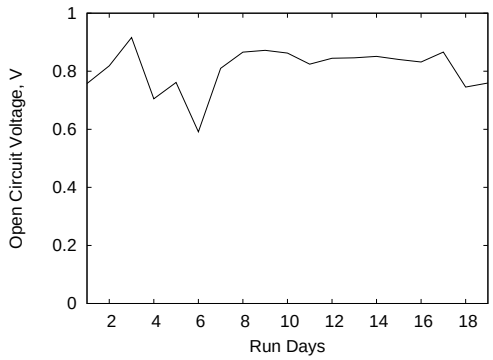

(a) Open Circuit Voltage, μ_1

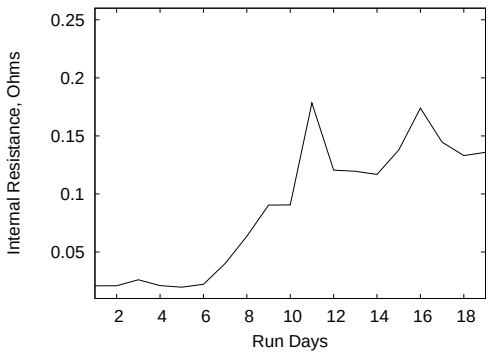

(b) Internal Resistance, μ_2

Figure 32: Parameters, μ_1 and μ_2, of equation (83) for the membrane given in Fig. 28(d) as a function of experiment run days.

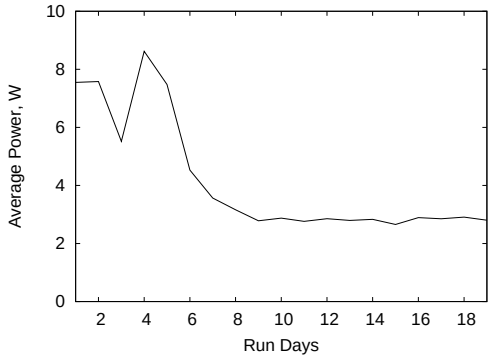

(a) Average Power for membrane 1

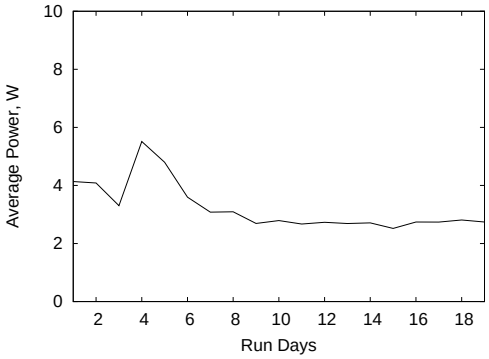

(b) Average Power for membrane 2

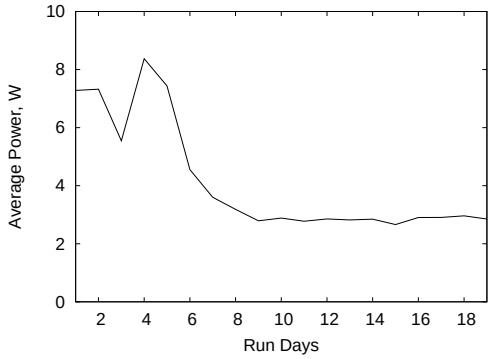

(c) Average Power for membrane 3

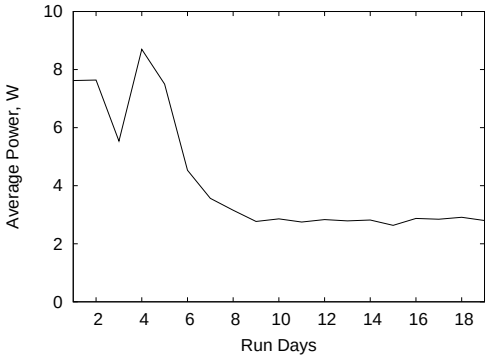

(d) Average Power for membrane 4

Figure 33: Average power for fourth set of four membranes in series as a function of experiment run days.

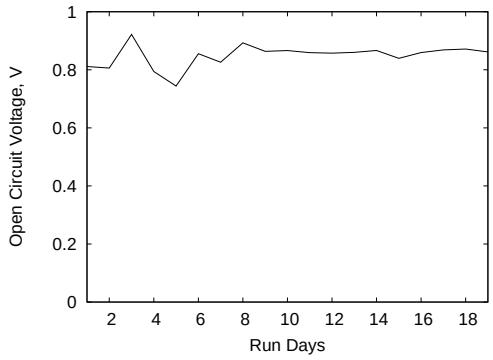

(a) Open Circuit Voltage, μ_1

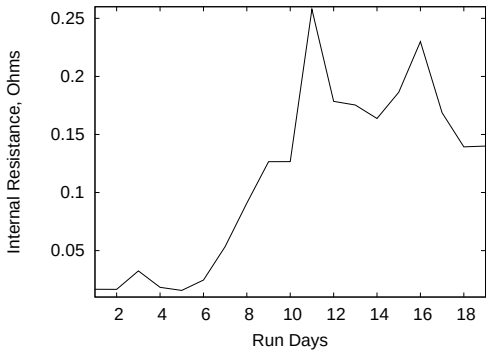

(b) Internal Resistance, μ_2

Figure 34: Parameters, μ_1 and μ_2, of equation (83) for the membrane given in Fig. 33(a) as a function of experiment run days.

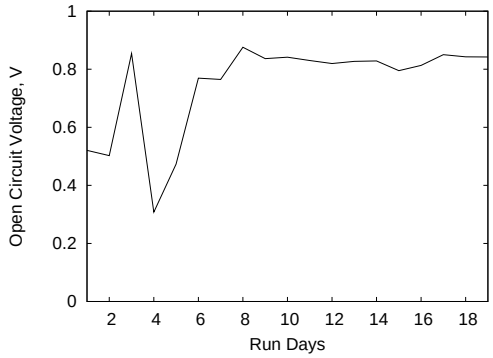

(a) Open Circuit Voltage, μ_1

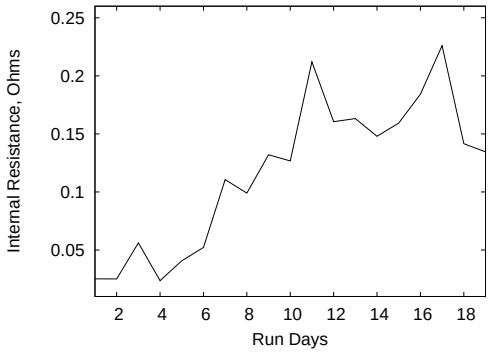

(b) Internal Resistance, μ_2

Figure 35: Parameters, μ_1 and μ_2, of equation (83) for the membrane given in Fig. 33(b) as a function of experiment run days.

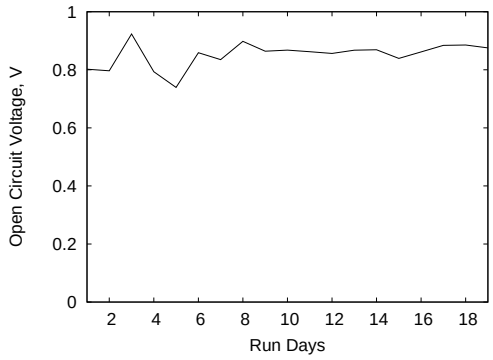

(a) Open Circuit Voltage, μ_1

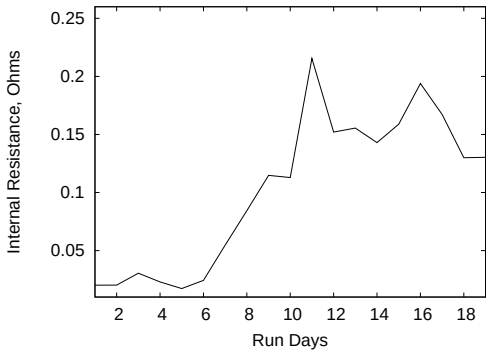

(b) Internal Resistance, μ_2

Figure 36: Parameters, μ_1 and μ_2, of equation (83) for the membrane given in Fig. 33(c) as a function of experiment run days.

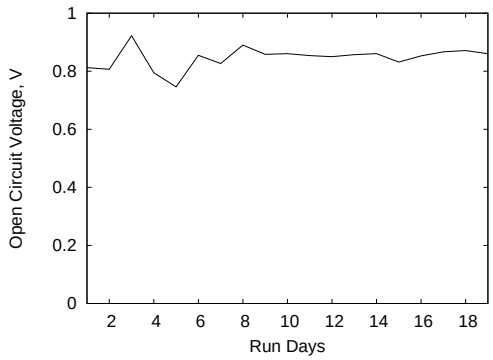

(a) Open Circuit Voltage, μ_1

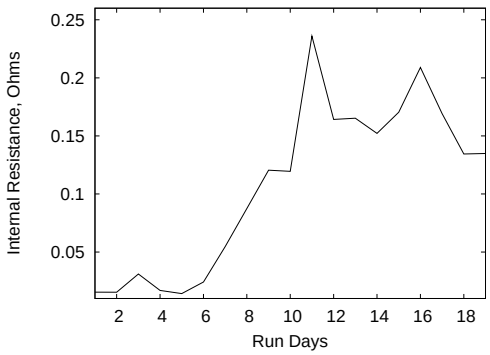

(b) Internal Resistance, μ_2

Figure 37: Parameters, μ_1 and μ_2, of equation (83) for the membrane given in Fig. 33(d) as a function of experiment run days.

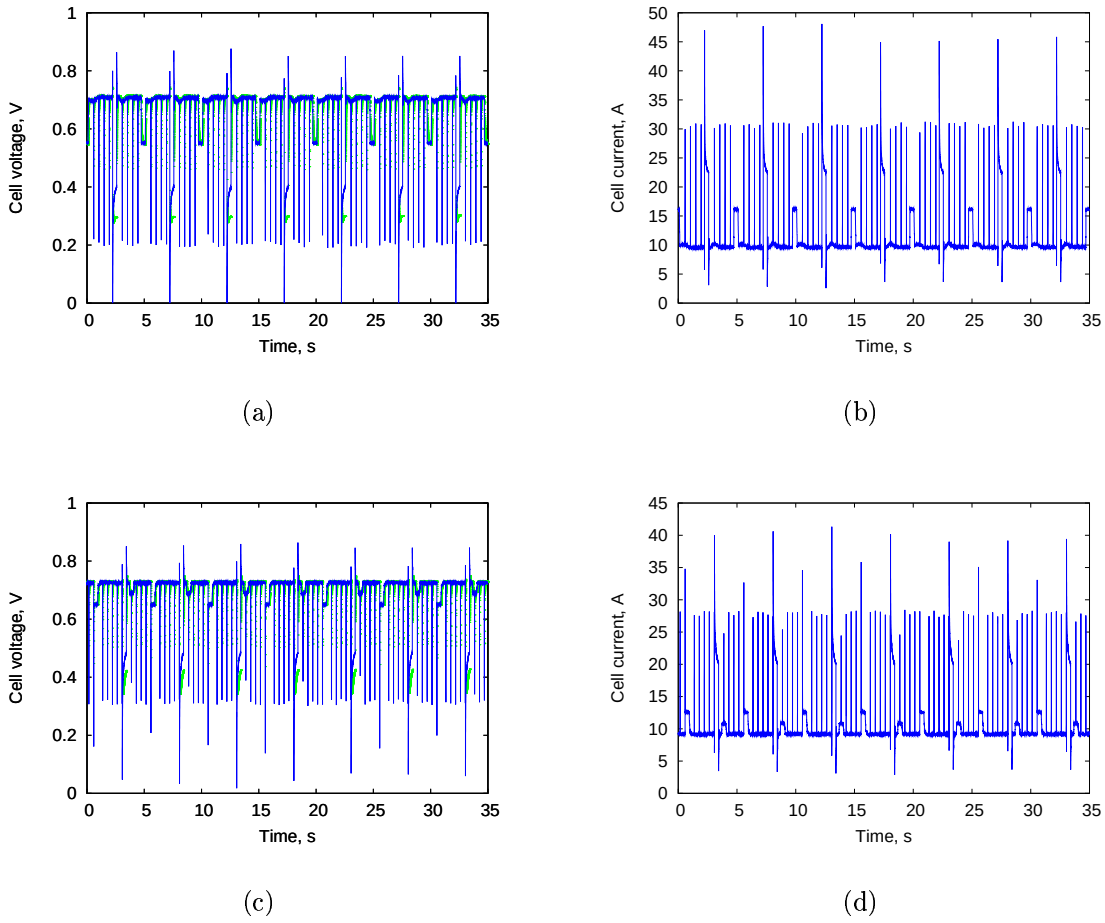

Figure 38: Measured (dots) and predicted cell voltage using the model in equation (83) in a) and c) for cell currents given in b) and d), respectively. The data and fits are for the membrane given in Fig. 28(a) before sixth experiment run day.

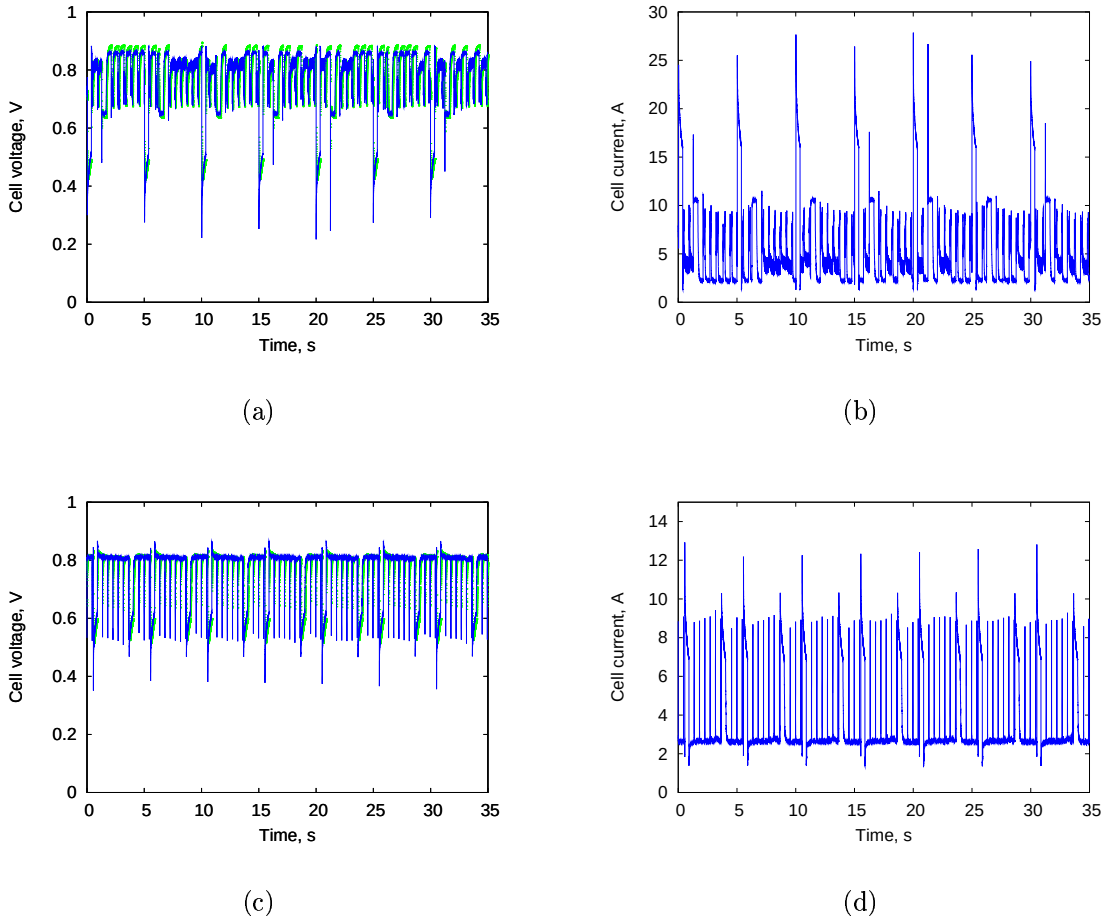

Figure 39: Measured (dots) and predicted cell voltage using the model in equation (83) in a) and c) for cell currents given in b) and d), respectively. The data and fits are for the membrane given in Fig. 28(a) on the sixth experiment run day, a) and b), and after sixth experiment run day, c) and d).

DISCUSSION

Accurate electrical terminal models of fuel cells are needed for integration of fuel cells with power electronics, critical loads, and control systems. This thesis presents a family of simple static and dynamic PEM fuel cell models that accurately describe PEM behavior even on cross-validation. Although developed with a small-signal formalism, the models appear to be useful for wide-ranging current and voltage responses with our experimental setup. The validated model (83) used for the describing membrane degradation provided significant results.

Several steady-state fuel cell models have been developed based on physical and empirical modeling. In this thesis static models are presented in the actual source notation, re-parametrized for identification and compared using experimental data. The proposed simple linear and quadratic models are used as benchmark to help assess relative usefulness of known models. The performance of all the considered static models and the proposed simple linear and quadratic models is comparable. There is a little reason to consider models that perform as well as the linear model but are more complex. This assertion is valid for the nature of experimental data collected in this thesis. There could be some situations, for example, varying gas pressure conditions, where a particular complex model might perform better.

This thesis proposes a physically motivated dynamic electrical terminal model of a proton exchange membrane (PEM) fuel cell obtained by extending a static current voltage description to include temperature dependence by dynamically modeling the temperature of the membrane. Model performance is validated using experimental data collected from a commercial PEM stack. The quality of fit for modeling voltage as a function of current, given the temperature measurements suggests thermal

response as a dominant pole for our stack. While temperature is a physically reasonable choice of state variable, there may be other good choices. For example, [8] models water concentration on the membrane as the important time-varying quantity. Some PEM systems include an external compressor that dominates the time response. The quality of fit evident in our results, even when our state variable corresponds to measured temperatures, is likely because temperature, humidity, and myriad other physical quantities are tightly linked in PEM fuel cells. The promising results from the dynamic modeling inspires the analysis of PEM fuel cell degradation through a model based approach.

The fuel cells are generally tested and modeled for constant DC loads for laboratory relevance only. In contrast, the PEM membrane degradation monitoring setup introduced in this thesis uses realistic, transient-rich load waveform. This type of investigation is required to understand difficulties encountered in practical applications of PEM fuel cells. For example, dynamic power requirement of the taxi in [33] suggests the use of transient loads in PEM fuel cell analysis. The proposed degradation setup makes continuous monitoring of individual membranes feasible.

The amount and complexity of the data present a challenge for model based analysis of degradation. Changes in persistence of individual membrane excitation precludes the use of complex models, so a simple model that can fit the degradation data for minimal excitation is used. The trends in the parameters of the linear resistive model over a period of time helped in recognizing two degradation modes. The degraded membranes failed approximately equally in these two modes.

Future work might include relating the electrical failure modes to the changes in membrane materials properties through techniques, for example, magnetic resonance microimaging, X-ray microimaging. Also, control systems including of transient detection strategies could be investigated to prevent degradation.

REFERENCES

[1] J. Padulles, G.W. Ault, and J.R. McDonald, "An integrated sofc plant dynamic model for power systems simulation," *Journal of Power Sources*, 2000.

[2] K. Sedghisigarchi and A. Feliachi, "Control of grid-connected fuel cell power plant for transientstability enhancement," in *IEEE Power Engineering Society Winter Meeting*, January 2002, vol. 1, pp. 383–388.

[3] J. Padulles, G.W. Ault, and J.R. McDonald, "An approach to the dynamic modelling of fuel cell characteristics for distributed generation operation," in *IEEE Power Engineering Society Winter Meeting*, January 2000, vol. 1, pp. 134–138.

[4] J. Padulles, G.W. Ault, C.A. Smith, and J.R. McDonald, "Fuel cell plant dynamic modelling for power systems simulation," in *34th Universities Power Engineering Conference*, September 1999, vol. 1, pp. 21–25.

[5] M.D. Lukas, K.Y. Lee, and H. Ghezel-Ayagh, "Development of a stack simulation model for control study on direct reforming molten carbonate fuel cell power plant," *IEEE Transactions on Energy Conversion*, 1999.

[6] M.D. Lukas, H. Ghezel-Ayagh, Mark C. Cervi, K.Y. Lee, and S.G. Abens, "Experimental transient validation of a direct fuelcell stack model," in *IEEE Power Engineering Society Summer Meeting*, July 2001, vol. 3, pp. 1363–1368.

[7] J.C. Amphlett, E.H. de Oliveria, R.F. Mann, P.R. Roberge, Aida Rodrigues, and J.P. Salvador, "Dynamic interaction of a proton exchange membrane fuel cell and a lead-acid battery," *Journal of Power Sources*, 1997.

[8] Wolfgang Friede, Stéphane Raël, and Bernard Davat, "Mathematical model and characterization of the transient behavior of a pem fuel cell," *IEEE Transactions on Power Electronics*, vol. 19, no. 5, pp. 1234–1241, September 2004.

[9] Peter Atkins and Julio de Paula, *Physical Chemistry*, W.H. Freeman and Company, 2002.

[10] D. Yu and S. Yuvarajan, "A novel circuit model for pem fuel cells," *Applied Power Electronics Conference and Exposition*, vol. 1, pp. 362–366, 2004.

[11] EGG Services Parsons Inc., "Fuel cell handbook (5th edition)," *DEO of Fossil Energy, National Energy Technology Lab*, 2000.

[12] Adrian Bejan, Ibrahim Dincer adn Sylvie Lorente, Antonio F. Miguel, and A. Heitor Reis, *Porous and Complex Flow Structures in Modern Technologies*, Springer, 2004.

[13] R. Kyoungsoo and S. Rahman, "Two-loop controller for maximizing performance of a grid-connected photovoltaic-fuel cell hybrid power plant," *IEEE Transactions on Energy Conversion*, vol. 13, no. 3, September 1998.

[14] D.J. Hall and R.G. Colclaser, "Transient modeling and simulation of a tubular solid oxide fuel cell," *IEEE Transactions on Energy Conversion*, vol. 14, no. 3, pp. 749–753, September 1999.

[15] K. Sedghisigarchi and A. Feliachi, "Dynamic model of a grid-connected solid oxide fuel cell (sofc)," in *Proceedings NAPS*, October 2002.

[16] S. Yerramalla, A. Davari, and A. Feliachi, "Dynamic modeling and analysis of polymer electrolyte fuel cell," *IEEE Power Engineering Society Summer Meeting*, vol. 1, pp. 82–86, July 2002.

[17] G. Squadrito, G. Maggio, E. Passalacqua, F. Lufrano, and A. Patti, "An empirical equation for polymer electrolyte fuel cell (pefc) behaviour," *Journal of Applied Electrochemistry*, vol. 29, no. 12, pp. 1449–1455, December 1999.

[18] J. Kim, S.M. Lee, S. Srinivasan, and C.E. Chamberlin, "Modeling of proton exchange membrane fuel cell performance with an empirical equation," *Journal of the Electrochemical Society*, vol. 142, no. 8, August 1995.

[19] G. Maggio, V. Recupero, and L. Pino, "Modeling polymer electrolyte fuel cells: An innovative approach," *Journal of Power Sources*, vol. 101, pp. 275–286, 2001.

[20] T.E. Springer, M.S. Wilson, and S. Gottesfeld, "Modeling and experimental diagnostics in polymer electrolyte fuel cells," *Journal of the Electrochemical Society*, vol. 140, pp. 3513–3526, December 1993.

[21] D.M. Bernardi and M.W. Verbrugge, "A mathematical model of the solid-polymer-electrolyte fuel cell," *Journal of Electrochemistry*, vol. 139, no. 9, pp. 2477–2490, September 1992.

[22] J.C. Amphlett, R.M. Baumert, R.F. Mann, B.A. Peppleyand P.R. Roberge, and T.J. Harris, "Performance modeling of the ballard mark iv solid polymer electrolyte fuel cell, ii. empirical model development," *Journal of the Electrochemical Society*, vol. 142, no. 1, pp. 9–15, January 1995.

[23] J.C. Amphlett, R.M. Baumert, R.F. Mann, B.A. Peppley, P.R. Roberge, and T.J. Harris, "Performance modeling of the ballard mark iv solid polymer electrolyte fuel cell, i. mechanistic model development," *Journal of the Electrochemical Society*, vol. 142, no. 1, pp. 1–8, January 1995.

[24] J. Hamelin, L. Agbossou, A. Laperriere, F. Laurencelle, and T.K. Bose, "Dynamic behavior of a pem fuel cell stack for stationary applications," *International Journal of Hydrogen Energy*, vol. 26, no. 6, pp. 625–629, June 2001.

[25] J.C. Amphlett, R.F. Mann, B.A. Peppley, P.R. Roberge, and A. Rodrigues, "A model predicting transient responses of proton exchange membrane fuel cells," *Journal of Power Sources*, vol. 61, pp. 183–188, 1996.

[26] Lu-Ying Chiu, Bill Diong, and Randall S. Gemmen, "An improved small-signal model of the dynamic behavior of pem fuel cells," *IEEE Transactions on Industry Applications*, vol. 40, no. 4, pp. 970–977, August 2004.

[27] G. A. F. Seber and C. J. Wild, *Nonlinear Regression*, Probability and Mathematical Statistics. Wiley, 1989.

[28] Rolf Johansson, *System Modeling and Identification*, Prentice Hall Information and System Sciences Series. Prentice-Hall, Englewood Cliffs, New Jersey, 1993.

[29] B. A. Boukamp, "A package for impedance/admittance data analysis," *Solid State Ionics*, pp. 136–140, 1986.

[30] N. A. Hampson, S. A. G. R. Karunathilaka, and R. Leek, "The impedance of electrical storage cells," *Journal of Applied Electrochemistry*, vol. 10, no. 1, pp. 3–11, 1980.

[31] P. D. Beattie, F. P. Orfino, V. I. Basura, K. Zychowska, J. Ding, C. Chuy, J. Schmeisser, and S. Holdcroft, "Ionic conductivity of proton exchange membranes," *Journal of Electroanalytical Chemistry*, pp. 45–46, January 2001.

[32] B. D. Cahan and J. S. Wainright, "Ac impedance investigations of proton conduction in nafion," *Journal of the Electrochemical Society*, vol. 140, December 1993.

[33] N. Schofield, H.T. Yap, and C.M. Bingham, "A H2 PEM Fuel Cell and High Energy Dense Battery Hybrid Energy Source for an Urban Electric Vehicle," in *IEEE International Conference on Electric Machines and Drives*, May 2005, pp. 1793–1800.

APPENDICES

APPENDIX A

ANALOG CONDITIONING BOARD SCHEMATIC

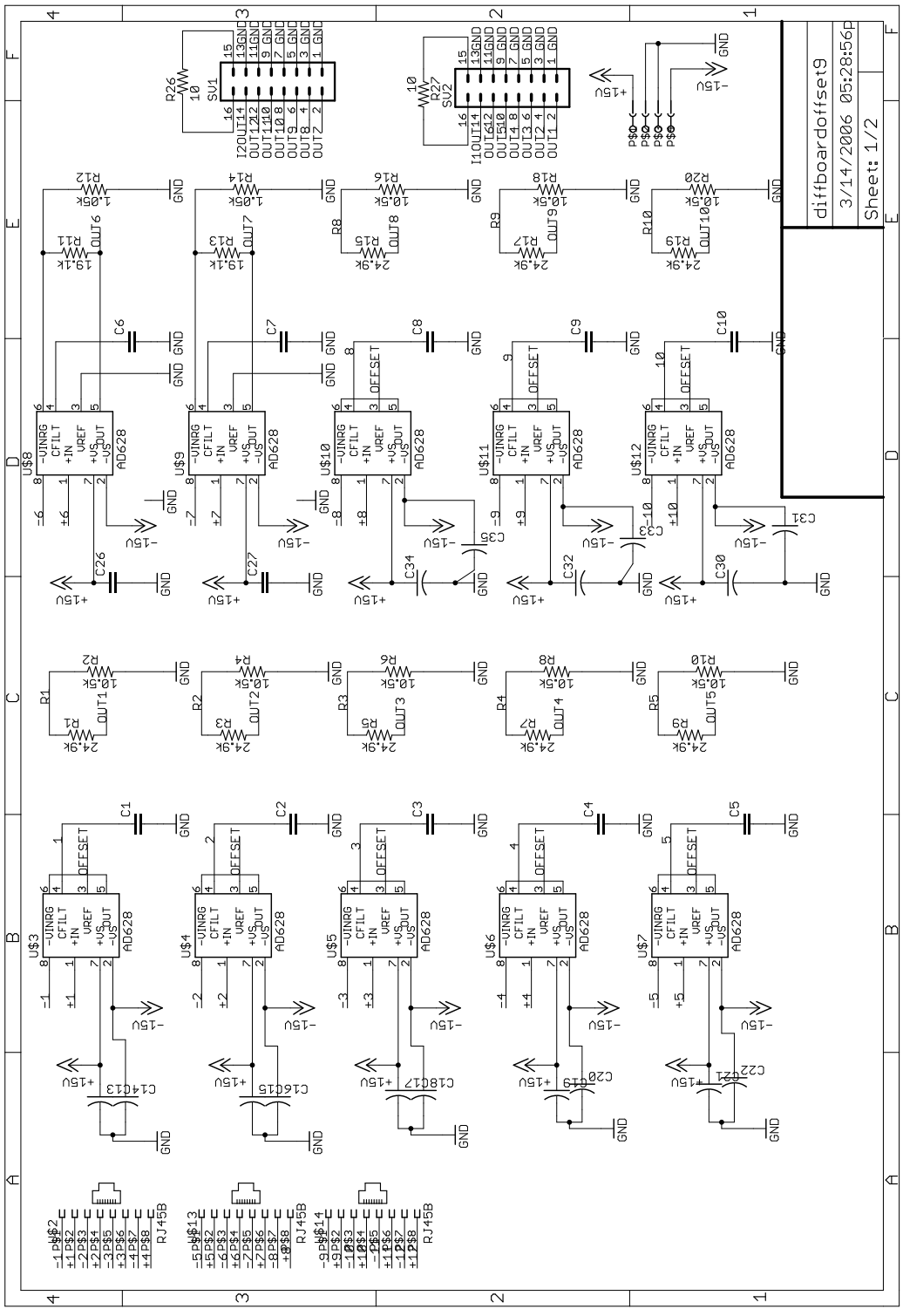
diffboardoffset9
3/14/2006 05:28:56p
Sheet: 1/2
AD628
RJ45B
+15V
-15V
GND

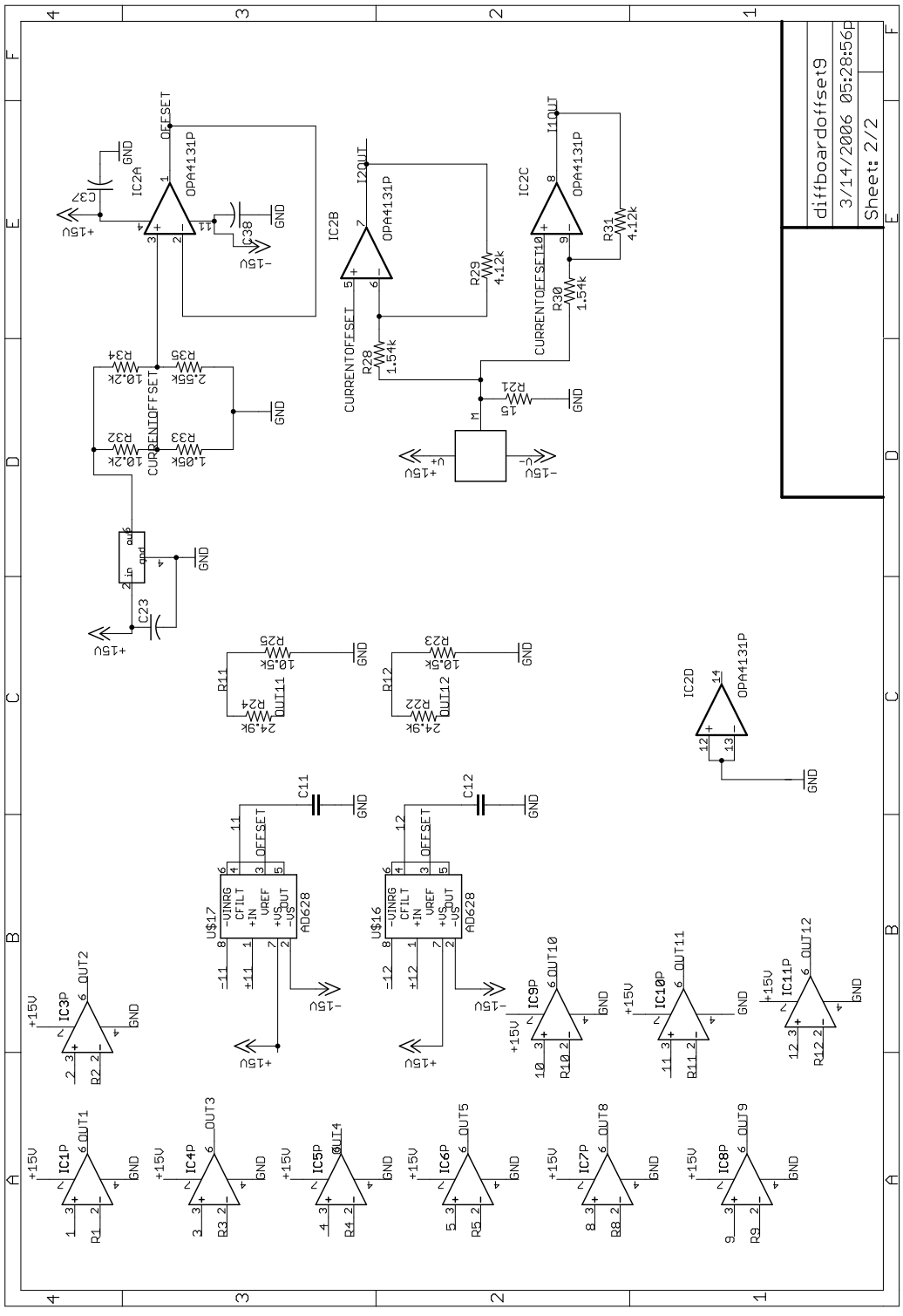
diffboardoffset9
3/14/2006 05:28:56p
Sheet: 2/2
IC2A
OPA4131P
OFFSET
C37
C38
GND
+15V
-15V
IC2B
I2OUT
R29
4.12k
IC2C
I1OUT
R31
4.12k
R30
1.54k
CURRENTOFFSET10
CURRENTOFFSET
R28
1.54k
R21
15
R32
10.2K
R33
1.05K
R34
10.2K
R35
2.55K
C23
IC2D
OPA4131P
R11
R24
24.9K
R25
10.5K
OUT11
R12
R22
24.9K
R23
10.5K
OUT12
C11
C12
U$17
U$16
AD628
-VINRG
CFILT
+IN
VREF
+VS
OUT
-VS
IC3P
OUT2
R2
IC1P
OUT1
R1
IC4P
OUT3
R3
IC5P
OUT4
R4
IC6P
OUT5
R5
IC7P
OUT8
R8
IC8P
OUT9
R9
IC9P
OUT10
R10
IC10P
OUT11
R11
IC11P
OUT12
R12

APPENDIX B

USB BOARD SCHEMATIC

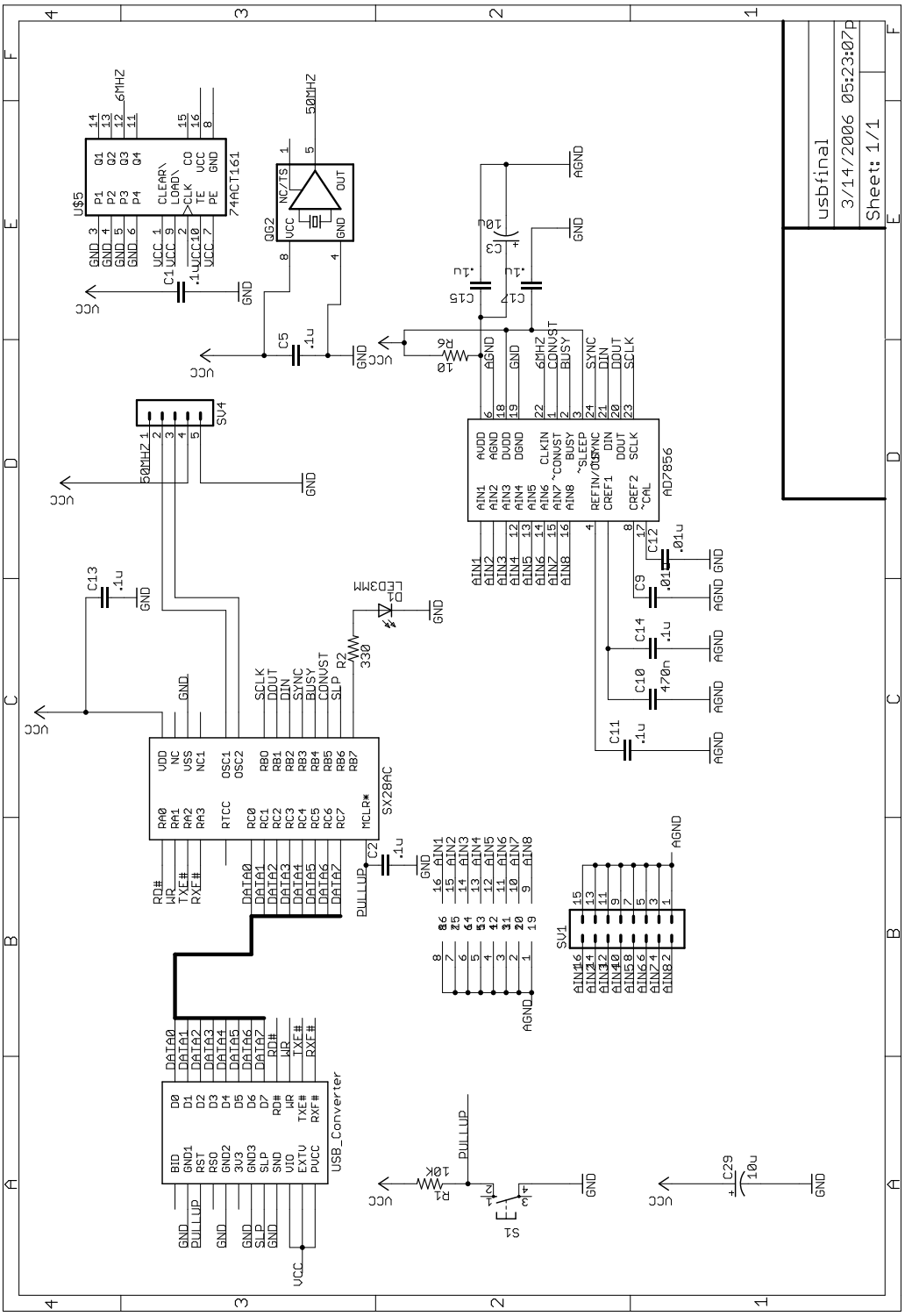
usbfinal
3/14/2006 05:23:07p
Sheet: 1/1
SX28AC
AD7856
USB_Converter
74ACT161
50MHZ
6MHZ
PULLUP
VCC
GND
AGND

APPENDIX C

USB CODE

```
; Code for USB interface Analog to Digital Converter
; S. R. Shaw  --  sshaw@alum.mit.edu
;
; Last revised:  March 22, 2003
;
; Added multiple channel capabilities.
;
;
;
device SX28L,oscxt5,turbo,stackx_optionx
id 'SX USB'
reset reset_entry
freq 48_000_000

;
;  Set the number of channels and frequency here.
;
; NUM_CHANNELS  is a literal between 1 and 8
;
; SAMPLE_DIV is a divisor that determines the net sampling frequency across
;  all channels, i.e. the sampling frequency per channel is the
;  net frequency divided by the number of channels
;
;               The net sampling frequency is   200 kHz / div
;
;  example: we want a 2kHz sampling frequency for 7 channels.
;  SAMPLE_DIV = 14 corresponds to a net sampling frequency of 14.285 kHz
;  The sampling rate per channel is therefore 2.040 kHz
;

NUM_CHANNELS = 7 ; Scan channels 1 through 7
SAMPLE_DIV = 14 ; Divisor for 2 kHz per channel


;
; Equates
;
usb_rxf = ra.3 ; input
usb_txe = ra.2 ; input
usb_wr = ra.1 ; output
usb_rd = ra.0 ; output
usb_data = rc ; port b  07?
usb_sleep = rb.6

adc_sclk = rb.0 ; communications clock for AD7856  (SX output)
adc_dout = rb.1 ; adc data out line    (SX input)
adc_din = rb.2 ; adc data in line     (SX output)
adc_sync = rb.3 ; sync for serial comm    (SX output)
adc_busy = rb.4 ; adc busy status line     (SX input)
adc_cnvst = rb.5 ; adc conversion start    (SX output)
```

```
LED = rb.7


;
; Variables
;
org 8h



ADC_lo ds 1 ; data to/from the ADC
ADC_hi ds 1

ADC_ch ds 1 ; Channel code

byte ds 1 ; used

string ds 1 ; used
temp ds 1
irq_count ds 1 ; used by the interrupt routine
irq_stat ds 1 ; lock out.


org 0
;
;
;; org 10h ;bank0 variables
;
;;extra = $
;
; org 30h ; bank 1 variables  (used as scratch by comparators)
; org 50h ;bank2 variables
;
org 0


;  interrupt routine
;
;  interrupt every 240 clocks, i.e. 200000 Hz
;
;  This routine requires a maximum of 10 clocks, minimum of 8 clocks
;
;  This is where all sample rates are set.
interrupt
djnz irq_count,end: ;2/4    execute every irq_div times
mov irq_count,#SAMPLE_DIV ;2 clocks

test irq_stat
snz
clrb adc_cnvst
```

```
inc irq_stat

end: mov w,#-240 ;1   interrupt every 240 clocks
retiw ;3 return


;
;
; Data
;
_start dw 'start',0
_stop dw 'stop',0
_cr dw 13,0
_hex dw '0123456789ABCDEF'

;
;
;***************
;* Subroutines *
;***************
;


;
; send_byte(byte), !(direction of RC)
;
; transmits the contents of byte via USB
;
send_byte
mov w,irq_stat
and w,#%11111110 ; is irq_stat bigger than 1?  If so, we've overflowed.
sz ; skip if irq_stat <= 1
clrb LED ; turn off LED indicating problems.
snb usb_txe ;
jmp send_byte

mode $0F ;change mode to write
mov !rc,#%00000000 ;port c

setb usb_wr ; hold usb_wr high
nop
mov w,byte
mov rc,w
nop
nop
clrb usb_wr
ret



get_byte
```

```
snb usb_rxf ; wait for data to be available from USB
jmp get_byte ; not yet ...

mode $0F
mov !rc,#%11111111 ; change mode to read.

nop ; 20 ns
clrb  usb_rd ; set RD# low
nop
nop ; 40 ns
mov w,rc
mov byte,w
setb usb_rd ; bring RD# high
ret

; this routine scans the input to match a string
; pointed to by w
match_string
mov string,w
:here mov w,string
mov m,#0
iread
mov m,#$F
test w
snz
ret ; return with z set, string is matched
mov temp,w
inc string
call get_byte
xor temp,byte
jz :here
ret ; return w/o z set, string fails to match



; Send string at w
send_string
mov string,w ;send string at w
:loop mov w,string ;read chr at w;
mov m,#0
iread
mov m,#$F
test w ;if 0, exit
snz
ret
mov byte,w
call send_byte ;not 0, send chr
inc string ;next chr
jmp :loop
```

```
; read/write from the ADC
;
;  This whole routine takes on the order of 16*280 ns = 4.5 us
;
;  Control data in [ADC_hi ADC_lo] is written to the device.  On
;  exit, ADC data from the conversion is in these same registers.
;

adc_io
clrb adc_sync ; clear ADC sync line
nop
nop ; Must provide setup for falling edge
nop

mov temp,#$08
here: rl ADC_hi ; put MSB of control word in carry
sc ; skip if carry
clrb adc_din ; MSB is zero, clear ADC data
clrb adc_sclk ; SCLK LOW  (delta = 7 cycles)
snc ; skip if not carry
setb adc_din ; MSB is one, set ADC data  (*)
nop ; pad so data access is 80ns after SCLK
stc ; set carry
sb adc_dout ; if data from ADC is 1, skip
clc ; input is zero, clear carry
setb adc_sclk ; SCLK HIGH (delta = 6 cycles)
djnz temp,here: ; 280 ns loop total = 3.6 Mhz

rl ADC_hi ; roll data into ADC_hi
setb temp.3 ; put 8 in count

there: rl ADC_lo ; put MSB of control word in carry
sc ; skip if carry
clrb adc_din ; MSB is zero, clear ADC data
clrb adc_sclk ; SCLK LOW  (delta = 7 cycles)
snc ; skip if not carry
setb adc_din ; MSB is one, set ADC data
nop ; pad so data access is 80ns after SCLK
stc ; set carry
sb adc_dout ; if data from ADC is 1, skip
clc ; input is zero, clear carry

setb adc_sclk ; SCLK HIGH (delta = 6 cycles)
djnz temp,there: ;

rl ADC_lo ; roll data into ax
setb  adc_sync ;
ret ;
```

```
;  send_hex(byte), !temp
; Send hex byte (2 digits) in arg
;
; uses:   for:
;-------------------
; arg     argument
; temp    internal storage
;
send_hex mov temp,byte
mov w,<>temp ;send first digit
call :digit

mov w,temp ;send second digit

:digit and w,#$F ;read hex chr
mov byte,w
mov w,#_hex
clc
add w,byte
mov m,#0
iread
mov m,#$F
mov byte,w
call send_byte
ret

;
; Main program
;
reset_entry

mode    $0F
mov ra, #%0011 ; set USB_WR and USB_RD default high
mov !ra,#%1100 ; set ra.0 and ra.1 as outputs

mov rc, #%00000000 ; initial state all low
mov !rc,#%11111111 ; set as inputs initially

mov rb, #%00101101 ; set initial state to avoid glitch
mov !rb,#%01010010 ; set inputs/outputs

clr fsr ; clear memory
loop: setb fsr.4
clr ind
ijnz fsr,loop:


setb LED ; turn LED on before calibration

:busy jb adc_busy, :busy ; wait for ADC calibration
mov ADC_hi, #%11100000 ; select control reg, single-ended, ch0, no power down
```

```
mov ADC_lo, #%00000000
clr ADC_ch
call adc_io ; put the AD7856 in some reasonable initial state

clrb LED ; turn LED off after calibration
mov !option,#%10011111 ; do real-time interrupt


; wait for USB setup here.
setup: ; Wait for setup information from the host
mov w,#_start ; look for this pattern to begin emitting data
call match_string ; try to match string
jnz setup: ; if z not set, string fails to match


setb LED ; turn the light on indicating that we're good so far
clr irq_stat ; clear the pending conversion, wait for new interrupt


:sync  test irq_stat
jz :sync

mov  ADC_hi, #%11100000
movb ADC_hi.4,ADC_ch.0
movb ADC_hi.3,ADC_ch.2
movb ADC_hi.2,ADC_ch.1

mov ADC_lo, #%00000000

setb adc_cnvst ; bring CNVST high (minimum 100ns pulse width)


:busy jb adc_busy,:busy ; Wait for ADC to finish conversion

call adc_io ; get the data, setup for next conversion

; We've got the data now, make sure we're not overlapping.

dec irq_stat
jz :skip
clrb LED ; turn LED off to indicate overflow.
jmp reset_entry ; data has been lost, start over with reclaibration
; and wait for start signal
clr irq_stat
:skip

; channel scan happens here

test ADC_ch
snz
setb ADC_hi.7 ; presently converting ch0, so data being sent
```

```
; is highest numbered channel.  Mark.

inc ADC_ch ; increment

stc ; get ready for CSB
csb ADC_ch, #NUM_CHANNELS ; if below NUM_CHANNELS == 1..8, skip.
clr ADC_ch


; Send out low ADC byte first, then hi
mov byte,ADC_lo
call send_byte
mov byte,ADC_hi
call send_byte

jmp :sync

;extra  code page
;ORG $400
```